UNIS
The University Centre in Svalbard

TU/e
EINDHOVEN
UNIVERSITY OF
TECHNOLOGY

Department of Applied Physics
Elementary Processes in Gas Discharges Research Group

Revealing the correlation between fat space weather and fat continuum emission

External Internship

Tim Hulsen

Supervisors:
Dr. Ir. Hjalmar C.J. Mulders
Prof. Noora Partamies

Draft version

Eindhoven, Month 20XX

Abstract

Auroral emissions consist of precise wavelengths that are produced by specific atomic and molecular transitions. Aurora-like emission with a continuous spectrum has been observed in Strong Thermal Emission Velocity Enhancement (STEVE) events equatorward of the auroral oval as the optical manifestation of sub-auroral ion drifts (SAIDs). Recently, spectrally continuous emission has also been observed in the auroral oval and, unlike STEVE, is correlated with auroral dynamics and particle precipitation. The list of known auroral continuum events is limited and lacks critical information on relevant space weather parameters to model possible mechanisms for generating continuous emission. In this work, we significantly extend the list of auroral continuum events by developing the first script that analyzes spectral images from the Meridian Imaging Svalbard Spectrographs (MISS) and detects continuous spectra. Two large-scale auroral continuum events are detected in the dayside aurora over Svalbard besides those previously reported by Partamies et al., additionally six continuum events of smaller scale are deteced over a range of magnetic local times. All four large-scale auroral continuum events are shown to occur for a shadow height between 100 - 200 km in the sunlit ionosphere. Furthermore, using the NASA OMNIWeb data explorer it is shown that all four events occur for solar wind speeds >550 km/s or a proton density of >8 n/cc and an auroral electrojet index (AE index) >200 nT. Considering these parameters, an additional four large-scale auroral continuum events are identified in all-sky camera images during similar ionospheric conditions and solar wind activity. Temporal evolution of the SYM/H index shows a negative deflection during all large-scale auroral continuum events, a signature of magnetic substorm activity. The AL index is also enhanced during all large-scale auroral continuum events, a possible treshold magnitude of -100 nT is identified. Evolution of the interplanetary magnetic field (IMF) components substantiates that the observed convection direction corresponds with the westward electrojet current, characterized by the AL index. Fluctuations in the B_z and B_y component are observed and hint at a correlation of aperiodic magnetic reconnection phenomena with dayside auroral continuum emission. Finally, satellites from the Defense Meteorological Satellite Program (DMSP) measure energy fluxes into the auroral oval corresponding with enhanced auroral electrojet magnitudes. This work shows that large-scale auroral continuum events in the dayside aurora are correlated with above average solar wind speeds or proton densities, enhanced ionospheric convection, the sunlit ionosphere and possibly magnetic reconnection phenomena, paving the way for future modelling efforts.

Preface

Please write all your preface text here. If you do so, don't forget to thank your supervisor, other committee members, your family, colleagues etc. etc.

Contents

Contents **iv**

1 Introduction **1**

2 Theory **3**

2.1 The Magnetosphere and Solar wind 3

2.1.1 The Magnetopause current & Magnetospheric cusp 4

2.1.2 The Magnetotail- & Ring currents 4

2.1.3 Ionospheric convection 6

2.2 Dayside aurora 7

2.2.1 Ion & neutral upwelling 7

2.2.2 The N_2+ ion in the sunlit ionosphere 8

3 Methods **9**

3.1 Kjell Henriksen Observatory (KHO) 9

3.1.1 Meridian Imaging Svalbard Spectrograph 10

3.1.2 Sony all-sky camera 10

3.2 Initial spectrograph data processing 11

3.2.1 Detecting auroral emission lines 11

3.2.2 Detecting possible auroral continuum emission 12

3.2.3 Results of initial data processing 13

3.3 Additional spectrograph data processing 13

3.3.1 Reducing noise and computing reference spectra 13

3.3.2 Filtering out false positives and final output 14

3.4 Defense Meteorological Satellite Program 14

3.5 NASA OMNIWeb data explorer 15

4 Results & Discussion **16**

4.1 Auroral continuum events 16

4.1.1 Fat events . . . 16
4.1.2 Thin and possible events . . . 17
4.1.3 Fake continuum events . . . 18
4.2 Continuum emission in the sunlit ionosphere . . . 19
4.2.1 Shadow height distribution of continuum events . . . 19
4.2.2 Ionospheric conditions surrounding continuum events . . . 20
4.2.3 Continuum event search based on ionospheric conditions . . . 22
4.2.4 Temporal evolution of ionospheric conditions . . . 23
4.3 DMSP satellite overpasses . . . 26
4.3.1 Satellite overpasses on 03-01-2020 . . . 27
4.3.2 Integrated energy fluxes . . . 27
4.3.3 Differential energy flux spectrogram . . . 28
4.3.4 Ion flow velocities . . . 30

5 Conclusion **31**

6 Outlook **33**

Bibliography **34**

Appendix **38**

A Spectrograph data processing **38**
A.1 Different populations . . . 38
A.2 Additional filtering methods MISS-1 . . . 40
A.3 False positives MISS-2 . . . 41

B Additional events **42**
B.1 Possible continuum events . . . 42
B.2 Fake continuum events . . . 44

C Additional analysis ionospheric conditions **45**
C.1 Keograms fat continuum events . . . 45
C.2 Temporal evolution ionospheric conditions . . . 46

Chapter 1

Introduction

We live in a society that has become increasingly dependent on satellites. One example is the use of the global positioning system (GPS). Navigation and monitoring of planes, ships and trains is all dependent on GPS [49]. Just recently, planes were grounded globally after a GPS glitch [39]. Currently, there are over 8000 satellites in orbit, with increasing privatization of the space industry this number is predicted to surge to 60,000 - 100,000 by 2030 [50]. This number of satellites can result in overcrowding of space and increases the risk of collisions which create millions of debris particles that are dangerous for other satellites [12].

Besides collisions, interactions of solar wind with Earth's magnetic field causes complex behavior of charged particles in the ionosphere that are known to incapacitate whole constellations of satellites. In 2022, 38 out of 49 Starlink satellites were lost during to a minor geomagnetic storm, the fate of 32 satellites was not tracked and the exact ionospheric process responsible for the failure of the satellites is unknown [19]. With more private companies launching satellites in Low-Earth Orbit (LEO) it is more crucial than ever to continue research on dynamic behavior in the ionosphere.

Figure 1.1: (Left) Photograph of STEVE taken on 03-09-2016 at 05:16 UT over Strathmore, Canada. North is to the right. [38]. (Right) Image of auroral continuum emission taken on 03-01-2020 at 08:48:56 UT over Longyearbyen, Svalbard.

Recently, new phenomena were identified in the ionosphere. A report in 2018 highlighted observations made by citizen scientists of a dynamic east-west aligned aurora-like structure equatorward of the region where auroras are expected [38]. One photograph of this phenomenon, so-called Strong Thermal Emission Velocity Enhancement or STEVE, is shown in

Figure 1.1. An unique property of STEVE is the observed white color, which is verified to be continuous emission over the entire visible spectrum [18]. Aurora-(like) emission is regularly not observed as a continuum but in colors corresponding to discrete emission lines from excited oxygen and nitrogen. Most dominant are the blue (427.8 nm), green (557.7 nm) and red (630.0 nm) auroral emission lines from the N_2+ ion and atomic oxygen.

As of yet, it is unclear how the continuum emission observed in STEVE is generated. STEVE has been identified to be an optical manifestation of extreme sub-auroral ion drifts (SAIDs) [1]. One hypothesis is based on a photochemical model that states that extreme ion velocities - over 4.4 km/s - in SAIDs paired with heating effects could excite N_2 to vibrational states leading to the formation of NO+. Nitricious oxide then reacts with ambient oxygen to produce NO_2 which is paired with continuum emission [20].

It has been determined that STEVE is not related to precipitation of particles from the magnetosphere into the ionosphere and is therefore not an auroral phenomenon [16]. In 2024, continuum emission was for the first time observed inside the auroral oval over Canada and Svalbard and the events appear to be closely related to auroral dynamics and particle precipitation, unlike STEVE [41, 46]. Figure 1.1 shows an image of continuum emission observed in the dayside aurora over Svalbard. Both Partamies et al. and Spanswick et al. have verified the continuous spectrum from spectrograph measurements [41, 46].

Partamies et al. also report a possible correlation of continuum emission with heating and upflow of ions in the dayside auroral oval, which could hint at a similar NO_2 continuum mechanism as proposed for STEVE [41]. But, besides the observations of Partamies et al. and Spanswick et al. there exists no further literature on continuum emission inside the auroral oval. There is a lack of known auroral continuum events and no extensive study regarding particle precipitation or other ionospheric conditions during these events. In this work, the goal is to extend the list of known auroral continuum events over Svalbard and investigate activity in the solar wind - magnetosphere - ionosphere coupled system amidst these events to pave the way for future modelling efforts.

This report is constructed as follows. Chapter 2 provides basic theory on relevant solar wind - magnetosphere - ionosphere coupled interactions and the dayside aurora. Chapter 3 elaborates on the first design of a script that automatically detects auroral continuum events in spectral images from the Meridian Imaging Svalbard Spectrographs (MISS) operated from the Kjell Henriksen Observatory (KHO) on Svalbard. The Defense Meteorological Satellite Program (DMSP) and NASA OMNIWeb data explorer used to study solar wind, magnetospheric and ionospheric conditions are also shortly highlighted. The main results of this work are provided and discussed in chapter 4. The number of known auroral continuum events similar to the event shown in Figure 1.1 is extended to eight, from the two events reported previously by Partamies et al. [41]. Several continuum events with a smaller spatial structure are also detected. All eight continuum events of similar structure are shown to occur for similar solar wind activity and ionospheric conditions in the dayside aurora, providing a novel insight into possible generation mechanisms. Conclusions are summarized in chapter 5 and an outlook for further research is given in chapter 6.

Chapter 2

Theory

In this chapter first a description of Earth's magnetosphere is provided. Dynamic interactions between the Sun and magnetosphere relevant for ionospheric conditions are elaborated. Special attention is given to the development of geomagnetic storms and ionospheric convection. Finally, a general description of the dayside aurora under the magnetospheric cusp region is given, highlighting features investigated in this work.

2.1 The Magnetosphere and Solar wind

Earth's magnetic field is in the simplest case depicted as a dipole field that is similar to the field of a bar magnet. This magnetic field originates from the motion of liquid in Earth's outer core [47]. Multiple complex variations exist within this dipole field, well known examples are the drift of magnetic poles and overall declining dipole field strength [53]. In this section we focus on variations induced by interactions with the Sun.

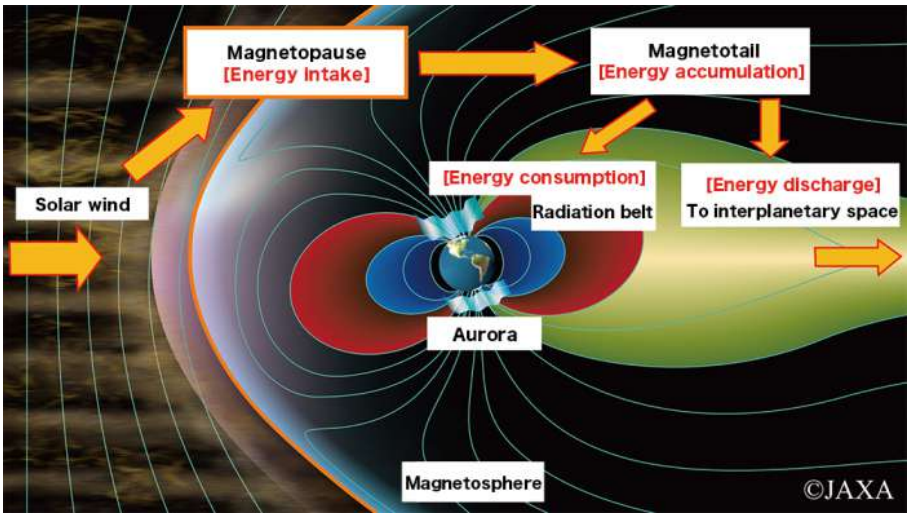

Figure 2.1: Flow of the solar wind around Earth's magnetosphere. Solar energy absorbed through the magnetopause circulates in the magnetosphere and generates the radiation belt and auroras. [21]

Figure 2.1 shows a general overview of Earth's magnetosphere. The magnetosphere consists of several key regions. The outer orange line in Figure 2.1 is the magnetopause, here

Earth's magnetic field is in balance with the pressure from the solar wind. As the solar wind is deflected around Earth's magnetic field it peels off and stretches field lines into a magnetotail. Both regions are important for the generation of auroras. Several dynamic processes at the magnetopause and magnetotail are elaborated in the next sections.

2.1.1 The Magnetopause current & Magnetospheric cusp

The solar wind consists of charged particles that impact on Earth's magnetic field. Charged particles are deflected from the magnetic field by the Lorentz force. As positively and negatively charged particles are deflected in opposite directions, rings of current develop around Earth's magnetic field, as shown in Figure 2.2. Magnetic fields induced by this current system cancel Earth's magnetic field outside the enclosed volume, known as the magnetosphere.

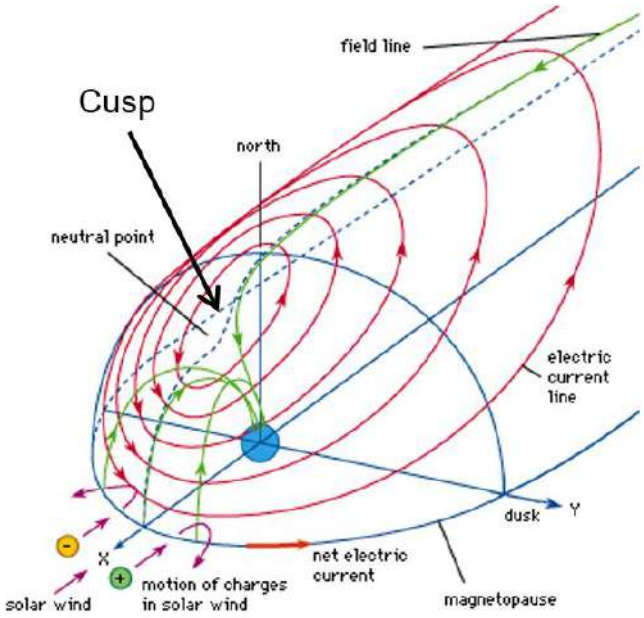

Figure 2.2: The northern part of the magnetopause current. Charged particles in the solar wind are deflected in opposite directions by Earth's magnetic field, creating a boundary current. This current confines the magnetosphere. Adapted from: [36].

Over the polar regions particles are not deflected at the neutral point but directly enter Earth's ionosphere along the converging magnetic field lines. The neutral point is known as the magnetospheric cusp. In the ionosphere below the cusp the solar wind particles induce dayside aurora with unique properties, this is further elaborated in section 2.2.

2.1.2 The Magnetotail- & Ring currents

Several other current systems exist besides the magnetopause current. Figure 2.3b shows the magnetotail current. The magnetotail current connects to the magnetopause current and similarly is generated by the deflection of charged particles along Earth's magnetic field lines. Earth's magnetic field and magnetotail current switch direction when crossing the equator, the return current closes the θ shaped magnetotail current loop in the equatorial plane. Deflected particles can turn back to Earth and are collected in the van Allen radiation belt, shown in Figure 2.1, or enter the ionosphere on the nightside, inducing the nightside aurora.

Another important current system is the westward ring current shown in blue in Figure 2.3a.

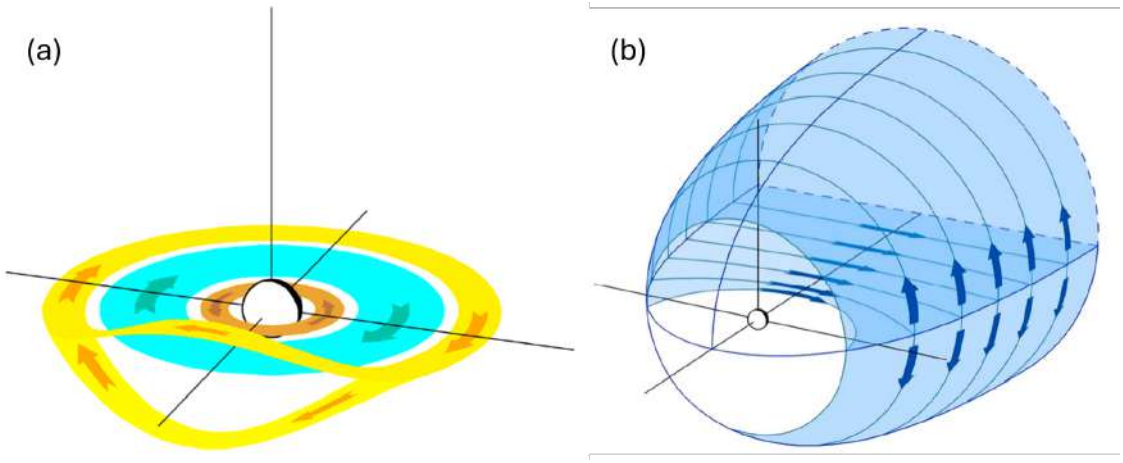

Figure 2.3: (a) The westward ring current in blue including the cut ring currents on the dayside in yellow. The eastward motion of electrons is shown in brown. (b) The magnetotail current with closure via the return current on the magnetopause. [17]

The cut ring current shown in yellow is outside the scope of this work. The ring currents are induced by a plasma pressure in the radiation belts resulting from collected hot particles [17]. During periods of increased solar winds a peak in plasma pressure develops and shifts towards earth, the onset of a magnetic storm. Resulting variations in the different ring currents are shown in Figure 2.4 as a function of time.

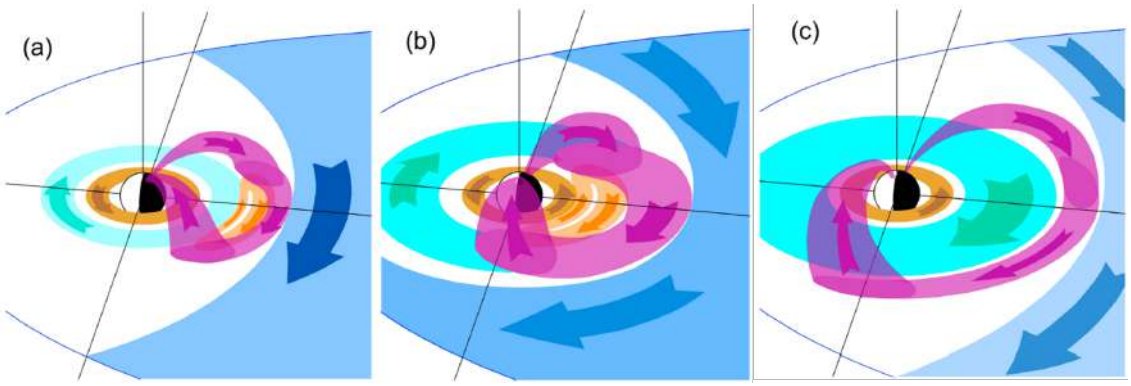

Figure 2.4: (a–c) Storm time transitions for the tail current (dark blue), banana current (orange), partial ring current (purple), symmetric ring current (light blue) and field-aligned currents connected to the partial ring current (purple). [17]

Figure 2.4a shows the configuration at the onset of a magnetic storm. The so-called banana current is centered around a localized peak in the plasma pressure in the radiation belt. As hot particles arrive on the nightside of the radiation belt, the westward ring current becomes asymmetric and forms the partial ring current that connects to the tail current and flows into the ionosphere along field-aligned currents.

As the solar wind magnitude increases, plasma is pushed along the magnetotail and into the radiation belts such that the plasma pressure increases, moving the pressure peak and the banana current inwards. Figure 2.4b shows the configuration during the main phase of a magnetic storm. The partial ring current merges with the westward ring current and field-aligned currents increase in magnitude, allowing hot particles to flow into the ionosphere. In the recovery phase - Figure 2.4c - the pressure peak becomes uniform around Earth and

a strong westward ring current remains. On Earth, the strength of the ring current is measured by variations in the magnetic field, known as the SYM/H index, and is used to follow the development of a magnetic storm [29].

2.1.3 Ionospheric convection

The magnetopause current and tail current, introduced in the previous sections, connect to the ionosphere through the region 1 and region 2 field-aligned currents, respectively, which are schematically shown in Figure 2.5. The field-aligned currents form a closed circuit through Pederson currents that flow anti-sunward over the polar cap. The magnetic field lines and associated currents induce an $E \times B$ drift in the ionosphere, resulting in ionospheric convection in two cells of opposite handedness [43]. The induced Hall current is greatest in the E-region of the auroral oval where a higher density of ions enhances conductivity. At higher altitudes, in the F-region, the density of particles is low such that ions experience little collisions and also move along the $E \times B$ drift. Ionospheric convection increases the temperature of ions and neutrals through frictional heating.

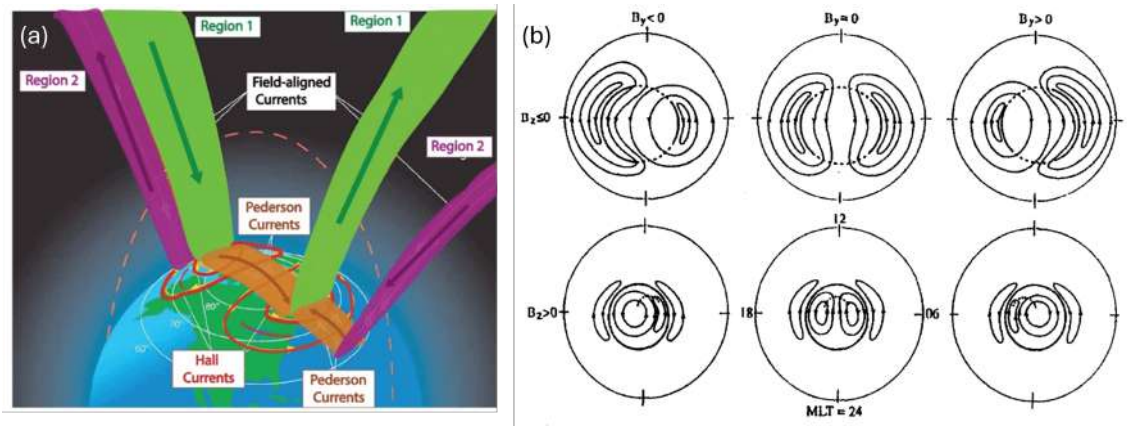

Figure 2.5: (a) Overview of the region 1 and region 2 field-aligned currents forming a closed current through the ionosphere following the Pederson currents. Induced Hall currents form the east- and westward ionospheric convection cells. [40]. (b) Schematic representation of ionospheric convection as a function of IMF direction. [6]

During magnetic storms the westward ring current increases in magnitude and enhances the region 2 field-aligned currents. Furthermore, during the main phase of a storm, an additional so-called wedge current develops between the magnetotail and ionosphere that drives into the westward electrojet centered around dawn, increasing its magnitude [17, 11]. The magnitude of the westward and eastward electrojet is measured by disturbances in the magnetic field at high latitudes, known as the AL and AU index, respectively. The AE index is defined as their difference and gives an indication for the overall auroral electrojet magnitude.

The B_z and B_y components of the interplanetary magnetic field (IMF) also influence the symmetry and magnitude of the auroral electrojets. In the case of negative (southward) B_z, Earth's magnetic field lines are anti-parallel to the IMF such that magnetic reconnection occurs on the dayside, the configuration assumed in previous figures. The polarity of the B_y component determines whether the reconnection point shifts towards dawn or dusk. In the case of $B_y < 0$ the dawn convection cell with eastward flow is enhanced, which strengthens the westward electrojet, as shown in Figure 2.5b. In the case of a northward B_z component reconnection occurs on the nightside and results in four-cell convection with opposite flow directions [6].

2.2 Dayside aurora

In this work the dayside or cusp aurora is of particular interest as Svalbard is one of the few ('easily' accessible) places on Earth located below the magnetospheric cusp, as shown in Figure 2.6a. The dayside aurora can be observed clearly during the polar night. It has been known for decades that the dayside aurora is significantly different than the nightside aurora. As mentioned in section 2.1.1, solar wind particles can directly enter the ionosphere through the cusp. These solar wind particles have less energy than those arriving on the nightside as they are not accelerated along the magnetotail. The dayside aurora is characterized by low-energy particle precipitation on the order of several hundred eV electrons and 1 keV protons, resulting in red (630.0 and 656.3 nm) and blue (486.1 nm) emission [23, 9]. An example of red-dominant dayside aurora above Svalbard is shown in Figure 2.6b.

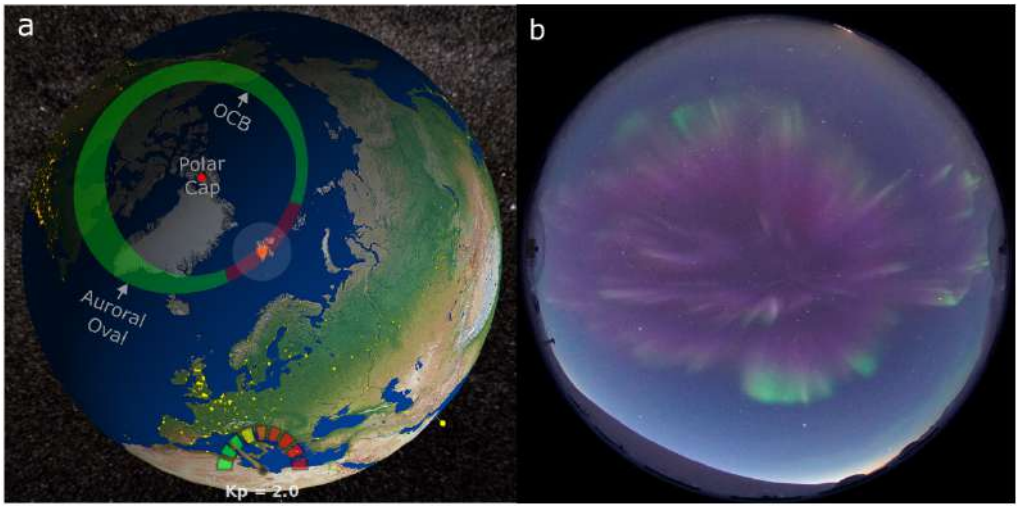

Figure 2.6: (a) Model of a contracted auroral oval at 08:00 UTC. The polar cap, auroral oval and open closed boundary (OCB) are indicated. The auroral oval is coloured green apart from the cusp region, which is coloured red. The red dots show the locations of geomagnetic north and Longyearbyen, Svalbard. The light-grey shaded area shows the optical horizon of an all-sky camera in Longyearbyen. (b) An all-sky image of red-dominant and pink dayside aurora above Svalbard. [23]

The cusp region is of interest in literature as it is the source of many dynamic auroral phenomena directly driven by the dynamics of magnetic reconnection [14, 23]. These phenomena are outside the scope of this work. In this section we focus on processes in the cusp region related to upwelling of nitrogen (ions) and the associated pink color - Figure 2.6b.

2.2.1 Ion & neutral upwelling

Several mechanisms result in the upflow of ions and neutral particles. One mechanism is related to the ionospheric convection discussed in the previous section. Ions drifting along the $E \times B$ direction in the F region penetrate into the E region of the ionosphere where they collide with other ions and neutrals. The resulting ion-neutral frictional heating results in vertical drift gradients that cause upward motion of both ions and neutrals [28]. Such shear flows can also occur locally and similarly cause upwelling of particles.

In the dayside aurora, there is another important mechanism. Low-energy precipitation ionizes the atmosphere at high altitudes (∼250 km), creating an electron pressure gradient that causes upflow of electrons from lower altitudes [10]. The upwelling electrons introduce a field-aligned ambipolar electric field that accelerates ions upward into the polar F region

ionosphere [28, 5]. Throughout the polar night the ionosphere is still sunlit above a certain altitude during daytime, schematically shown in Figure 2.7a. The altitude above which the ionosphere is sunlit is called the shadow height. Direct exposure to solar extreme ultraviolet (EUV) radiation causes photoionization in the sunlit region of the ionosphere and similarly induces an ambipolar electric field that results in the upflow of ions [28, 5]. Both low-energy precipitation and photoionization have been shown to also result in the upflow of neutral particles.

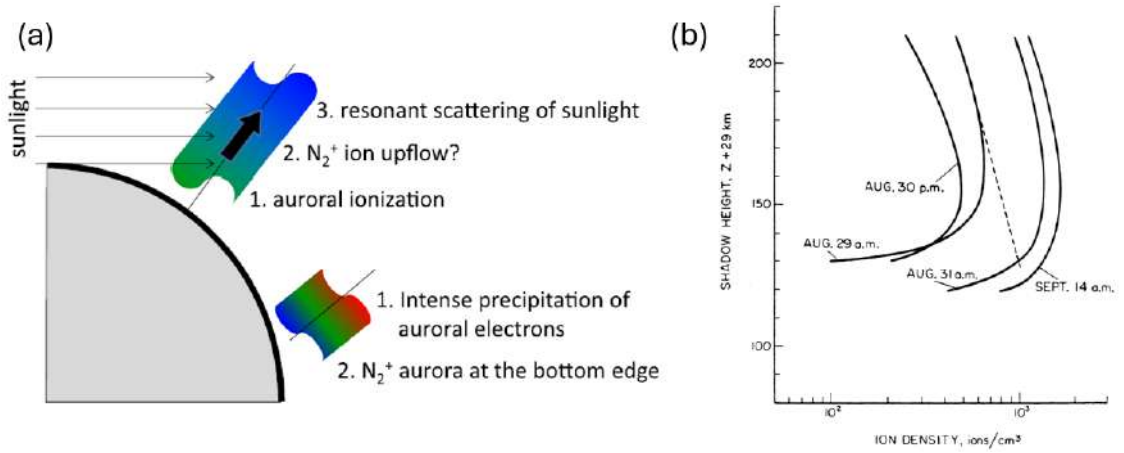

Figure 2.7: (a) Schematic of two types of auroral N_2+ emission caused by intense electron precipitation on the nightside and resonant scattering of sunlight by N_2+. Adapted from [45]. (b) N_2+ density in low-altitude sunlit aurora for four twilights in 1960. The dashed line is an estimate of the N_2+ density assuming losses through dissociative recombination. [25]

2.2.2 The N_2+ ion in the sunlit ionosphere

In this work molecular nitrogen and the N_2+ ion are of particular interest as continuum emission observed in STEVE is predicted to originate from the formation of NO_2 from molecular nitrogen, as stated in the introduction. Emission from N_2+ is observed frequently in the sunlit ionosphere over Svalbard [10].

In the dayside aurora the density of molecular nitrogen and N_2+ increases at higher altitudes due to upflow discussed in the previous section. Furthermore, additional N_2+ is produced at from the upflow of molecular nitrogen by direct ionisation via electron impact or by photoionization above the shadow height,

$$N_2 + e \longrightarrow {N_2}^+ + e + e' \tag{2.1}$$

$$N_2 + h\nu(<79.6\text{ nm}) \longrightarrow {N_2}^+ + e, \tag{2.2}$$

where e' is a thermal electron and $h\nu$ the EUV photon energy [10, 25]. Figure 2.7b shows the density of N_2+ for different shadow heights, indicating a clear peak in the ion density around a shadow height of 150 km. Short wavelengths (∼75 nm) in the EUV spectrum penetrate deep into the ionosphere to roughly 150 km [15]. The majority of the EUV spectrum is attenuated by at least 1/e below 150 km [10].

The production of N_2+ is observed on the nightside during intense particle precipitation as blue or purple aurora at low altitudes, where there is an abundance of nitrogen [45], as depicted in Figure 2.7a. In the dayside aurora purple (or pink) emission is observed at high altitudes and indicates the upflow of nitrogen. The intensity of emission by N_2+ can be enhanced by a factor of 100 during dayside aurora due to solar fluorescence in the sunlit ionosphere [25, 10].

Chapter 3

Methods

In this chapter the methods used to obtain the results of this work are described. The first section describes the Meridian Imaging Svalbard Spectrographs, MISS-1 and MISS-2, and their capabilities. The Sony all-sky camera used to capture images is also shortly highlighted. The second section describes initial data processing methods used to detect possible auroral continuum events. The third section describes data analysis methods used to filter out events that do not show clear auroral activity. Addtional sources of data, such as ionospheric data from the Defense Meteorological Satellite Program (DMSP) and solar wind data from the NASA OMNIWeb data explorer, are described in sections four and five, respectively.

3.1 Kjell Henriksen Observatory (KHO)

The equipment in this work is operated from the Kjell Henriksen Observatory (KHO) in Svalbard. Figure 3.1 shows a bird's eye view of KHO and nearby EISCAT radars on top of the mountain Breinosa (78.2° N, 15.6° E). The location of KHO is ideal for auroral observations, as it is located under the dayside cusp - see section 2.2 - high above the Arctic Circle where the polar night lasts from November to February. The high altitude of KHO (520 m) allows for a full field of view (FOV) of the sky and minimizes light pollution from the city of Longyearbyen.

Figure 3.1: A bird's eye view of the Kjell Henriksen Observatory. The EISCAT Svalbard Radar antennas can be seen behind the observatory. The road through the Adventdalen valley is also visible, which leads to the town of Longyearbyen in the top left of the image. [24]

3.1.1 Meridian Imaging Svalbard Spectrograph

The Meridian Imaging Svalbard Spectrograph prototypes MISS-1 and MISS-2 are hyperspectral pushbroom imagers based on the same design [26]. Figure 3.2 shows MISS-2 in one of the domes on the roof of KHO, together with the Sony A7s all-sky camera - highlighted in the next section. See the master thesis of Nicolas Martinez for an elaborate description of the optical design of MISS and theoretical background [34]. For this work it is important to note that both spectrographs use an all-sky lens to capture incident light in a 180° FOV onto an entrance slit. Only a narrow strip of light along the geomagnetic meridian passes through the slit, indicated by the white rectangle in the right image of Figure 3.2.

Figure 3.2: (Left) Image from inside the dome located on the roof of the Kjell Henriksen Observatory that hosts the Sony A7s all-sky camera and Meridian Imaging Svalbard Spectrograph (MISS-2). (Right) Image taken by the Sony A7s camera on 22-12-2024 at 09:28:30 UT. The white rectangle indicates the field of view of MISS-2 along the magnetic meridian.

MISS-1 started operations in 2018 and has gathered data every winter season from roughly November to February, including some days in October and March in 2020 and 2023, until November 2024 when MISS-2 was installed. MISS-1 and MISS-2 have slightly different specifications. Data captured by MISS-1 has a angular resolution just above 1° and time resolution of 1 frame/minute. MISS-1 was slightly out of focus before the installation of MISS-2, resulting in a spectral resolution between 1 - 2 nm. MISS-2 has a similar angular resolution, but higher time resolution of 4 frames/minute and spectral resolution of roughly 1 nm. Both have a spectral range of 400 - 700 nm.

3.1.2 Sony all-sky camera

The Sony A7s all-sky camera is positioned next to MISS - as shown in Figure 3.2. The camera has a full 180° FOV lens with a 12 megapixel sensor and 4 second exposure time [27]. The time resolution is roughly 6 frames/minute. The camera is used to capture images of the entire sky, including auroras, clouds and stars. The images are used to determine the location of auroras in the sky for satellite overpasses and to filter out false positive events in the data analysis. Images of auroras in RGB colors can be compared to spectral images from MISS to determine the color and type of aurora. The Sony A7s camera has been in operation since November 2015 and has captured images every winter from October to March.

3.2 Initial spectrograph data processing

In order to investigate possible sources of auroral continuum emission, as stated in the introduction, it is desired to extend the number of known auroral continuum events such that correlations can be made with e.g. solar- or ionospheric activity. In this section an overview is given of initial data processing methods used to detect possible auroral continuum events in the large amount of data gathered by MISS-1 and MISS-2.

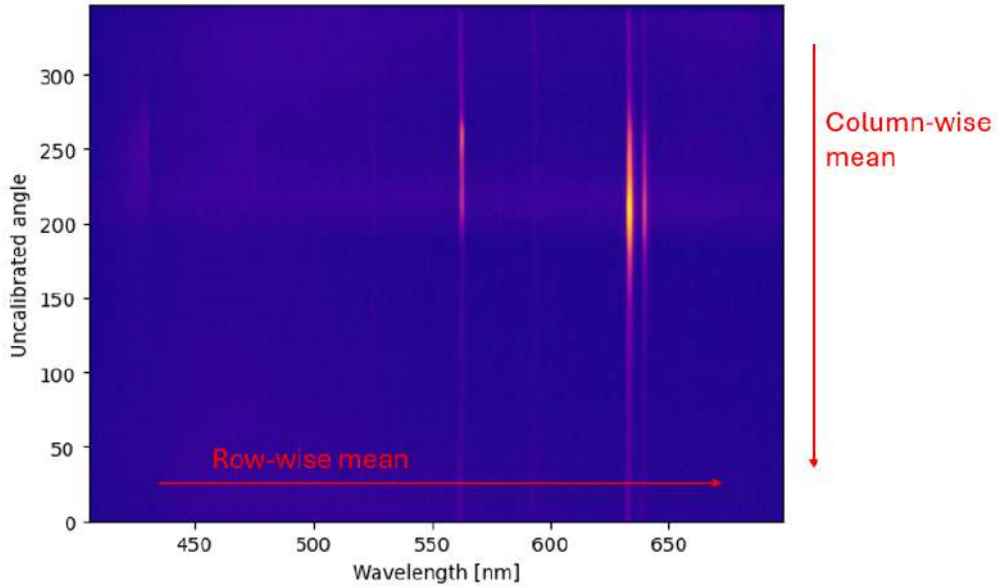

Figure 3.3: Spectral image taken by the Meridian Imaging Svalbard Spectrograph 2 on 22-12-2024 at 09:28:30 UT. The x-axis shows the spectral range from 400 - 700 nm divided over 1039 columns - pixels of the CCD sensor. The y-axis shows the expected angle of the incoming light. The northern horizon is at the bottom of the image. The brighter the pixel, the more light is captured of a specific wavelength. Red arrows indicate the direction of computing the column- and row-wise mean.

Initial data processing is done to greatly reduce the amount of data to be analyzed in more detail. With a time resolution of 1 frame/minute MISS-1 captures roughly 172.800 spectral images per season. MISS-2 captures four times as much in a season. It is expected that only a small fraction of these images contain auroral events at all, simply due to auroral inactivity and cloud cover. Spectral images are saved for further analysis based on two assumptions: (1) the green (557.7 nm) and red (630.0 nm) auroral emission lines are distinctly visible in the spectral image, ensuring that there is auroral activity, and (2) there is a distinct peak in the row-wise mean of the spectral image. Assumption 2 is an early indicator of spectral enhancement over the full spectral range characteristic for continuum emission - see section. Initial processing based on these assumptions is now elaborated in more detail for MISS-2. An earlier version of this method was used for MISS-1 where also the blue (427.8 nm) auroral emission line is considered in assumption (1). See the full code on GitHub cite.

3.2.1 Detecting auroral emission lines

Figure 3.3 shows the spectral image taken by MISS-2 at the same time as the image taken by the Sony A7s camera in Figure 3.2. The brightness of the pixels in the image is a measure for the number of counts captured by the CCD sensor for a specific wavelength along the slit facing the geomagnetic meridian. First, the column-wise mean is computed by averaging

the number of counts over all rows for each column. The result is shown in Figure 3.4a. The average number of counts is plotted as a function of wavelength. The SciPy peak finding function is used to detect peaks of a minimum prominence and width. The prominence is defined as the vertical distance between the peak and its lowest contour line, the lowest horizontal line that intersects the signal again or reaches the window border - see Figure 3.4b. These parameters have been arbitrarily set by comparing different auroral events and clear skies. In the future these parameters can be optimized by performing a statistical analysis of MISS data with and without auroral activity. See the full code on GitHub for the specific parameters and user-defined functions used in this work cite. Detected peaks are highlighted with red dashed lines in Figure 3.4a, showing that the green and red auroral emission lines are clearly visible. Files are removed from further analysis if the green and red emission lines are not detected.

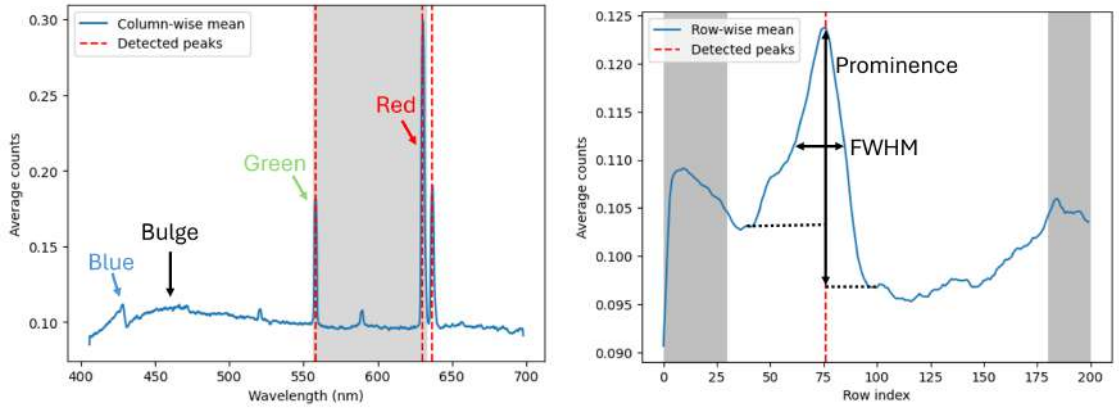

(a) Column-wise mean

(b) Row-wise mean

Figure 3.4: (a) Column-wise mean of the spectral image shown in Figure 3.3. The average number of counts is plotted as a function of wavelength. The light grey shaded area is considered for computing the row-wise mean. The blue, green and red auroral emission lines are highlighted as well as the observed bulge. (b) Row-wise mean within the light grey shaded area of (a). The average number of counts is plotted as a function of the row index. Dark grey shaded areas are omitted. The full width at half maximum (FWHM) and prominence are highlighted. The red dashed lines in (a) and (b) indicate peaks detected with a scipy peak finding function.

3.2.2 Detecting possible auroral continuum emission

A bulge can be seen in the column-wise mean around 460 nm. This is likely due to the presence of blue skies seen in Figure 3.2. This bulge can be even more pronounced in the case of sunlit clouds, see Figure A.3, and mimics the spectral enhancement seen for continuum emission. Therefore, in the next step, the row-wise mean is computed by averaging the number of counts for each column within the range highlighted by the light grey shaded area in Figure 3.4a. It is expected that in this range the influence of blue skies or clouds is minimal. Data from MISS-1 was analyzed in an earlier stage of this work when the full range of columns was considered for computing the row-wise mean.

The row-wise mean is shown in Figure 3.4b. The average number of counts is plotted as a function of the row index, or the angle of the incoming light. Again the SciPy peak finding function is used to detect peaks. The first 30 and last 20 rows, highlighted by grey shaded areas, are not considered for peak detection. The intensity of incoming light drops at the edges of the CCD sensor, or conversely, increases significantly at the edges due to the sun moving along the southern horizon. It is shown that a peak is detected for row index 76,

highlighted with the red dashed line. This row index corresponds to the enhanced spectral emission seen over the full spectral range in Figure 3.3 between 200 - 250 degrees. This angle coincides with the auroral continuum event in Figure 3.2, validating that this initial processing method can succesfully detect auroral continuum emission. Again, a spectral image is removed from further analysis if no peak is detected in the row-wise mean.

3.2.3 Results of initial data processing

The initial data processing described above is effective in filtering out most of the data that does not show possible auroral continuum events. From the 613,691 spectral images captured by MISS-1 between 2020 - 2024, only 3860 are saved for further analysis. Data from the first years of operation of MISS-1 is affected by dust on the CCD sensor. For 2018 only data from December is used, for 2019 all data is used but most is removed during initial processing. From the 517,890 spectral images only 789 are saved.

MISS-2 has captured 581.113 spectral images from 27-09-2024 to 26-02-2025, 13,765 are saved for further analysis. However, there is an issue with horizontal and slightly diagonal lines in spectral images from MISS-2 - see Appendix A.3. These lines are falsely detected as possible continuum emission and are found to occur mostly in sunlit and cloudy conditions, but also for clear skies. In this work, days have been partially excluded based on roughly the hourly conditions visible in Sony A7s images and corresponding spectral images. This reduces the number of events saved for further analysis to 2085. In the future, initial data processing can be improved to exclude sunlit and cloudy conditions such that little filtering by hand is required when the amount of available data increases next season.

3.3 Additional spectrograph data processing

The spectral images saved in initial processing are stored in text files in a combination of filename and the detected row index, shown in Figure 3.4b. In this section additional processing steps are elaborated that are used to visualize detected events and filter out remaining false positives that do not show clear auroral emission due to e.g. clouds or sunlit conditions.

3.3.1 Reducing noise and computing reference spectra

Auroral events, such as shown in Figure 3.2, are expected to be visible over a range of rows in a spectral image. Several rows have to be considered in order to compute a representative spectrum with little noise. In this work an average spectrum is computed over a range of rows equal to the full-width-half-maximum (FWHM) of the peak detected in the row-wise mean. In this way a consistent method is used to determine the spectrum of each unique auroral event. The FHWM is determined with the SciPy peak widths function cite. Figure 3.5 shows the same spectral image shown earlier in Figure 3.3 where now the blue dashed line indicates the row of the peak detected in Figure 3.4b. The spectrum corresponding to this row and averaged over the FWHM of the detected peak is also shown in averaged counts as a function of wavelength.

Next, a reference spectrum is computed to determine the spectral enhancement characteristic for auroral continuum emission. Ideally, the reference spectrum consists of clear skies, however, this is not always possible in the case of large auroral events or cloud-cover. In this work the reference spectrum is defined as the average spectrum with minimum emission or counts. The simple rolling average of the row-wise mean, shown in Figure 3.4b, is computed with a window equal to the FWHM of the detected peak. Then, the minimum value of the rolling average is determined and the corresponding row index is used to compute the averaged reference spectrum over a range of rows equal to the FWHM. By using this method it is ensured that the reference spectrum is computed over the same range of rows as the detected spectrum with minimum emission in that range. The row corresponding to

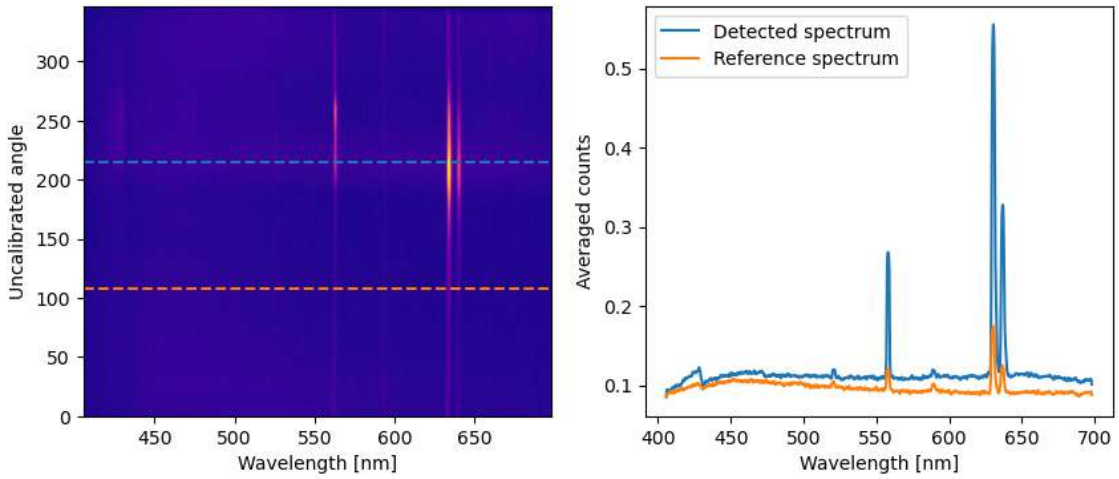

Figure 3.5: (Left) Spectral image taken by the Meridian Imaging Svalbard Spectrograph 2 on 22-12-2024 at 09:28:30 UT shown in Figure 3.3. The blue dashed line indicates the row index of the peak detected in Figure 3.4b. The orange dashed line indicates the row with minimum emission. (Right) The spectrum along the detected row index averaged over a range of rows equal to the FWHM of the detected peak (blue). The reference spectrum along the row of minimum emission averaged over the same range of rows (orange).

the reference spectrum is highlighted in Figure 3.5 with the orange dashed line. The averaged reference spectrum is also shown in averaged counts as a function of wavelength. The spectral enhancement of the detected spectrum from the auroral continuum event shown in Figure 3.2 is clearly visible when compared to the reference spectrum.

3.3.2 Filtering out false positives and final output

In the 4649 events from MISS-1 and 2085 events from MISS-2 that have passed initial processing there exist some 'false positives' that do not show clear auroral emission but instead show, for example, clouds reflecting moonlight. The number of false positives is small for MISS-2 as files had already been removed based on the conditions visible in Sony A7s images. It is described in Appendix A how additional filtering methods were used for MISS-1 and different populations of events are defined for both spectrographs. This is not elaborated here as it is not relevant for the results presented in the next chapter.

Final filtering is conducted for both spectrographs by matching the spectral images with Sony A7s images taken closest in time cite. The Sony A7s images are hand filtered based on visible cloud-cover or sunlit conditions in combination with the detected spectra. The remaining Sony A7s images are paired with the spectral images to obtain a final selection of events. The final output consists of pdf files where each page shows the spectral image, detected spectrum and reference spectrum as shown in Figure 3.5 together with the corresponding Sony A7s image as shown in Figure 3.2 with blue- and orange dashed lines indicating where in the sky the detected- and reference spectrum are captured.

3.4 Defense Meteorological Satellite Program

The DMSP consists of several satellites in a 101 minute, near-polar orbit at an altitude of 830 km. These satellites regularly pass directly over Svalbard in the morning hours or around noon. Each satellite is equipped with sensors that record along-track plasma densities, velocities, composition, drifts and temperature in the ionosphere [13]. In this work these

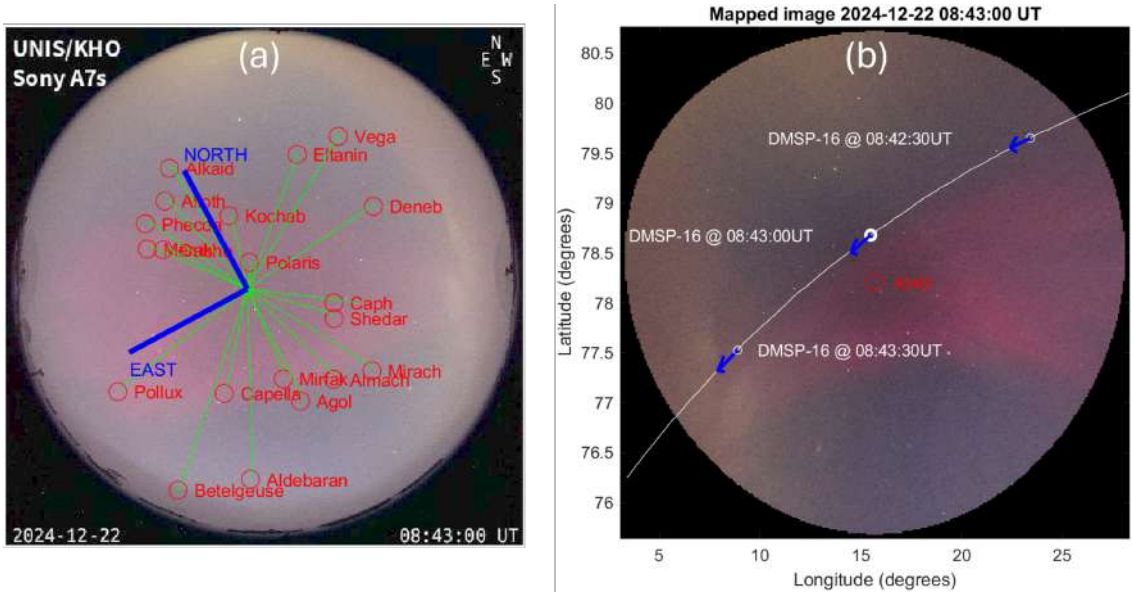

Figure 3.6: (a) Sony A7s image taken on 22-12-2024 at 08:43:00 UT overlayed with a sky chart of 20 identified stars. The position of the stars is known and used to determine the zenith and geographical north and east. (b) Based on the sky chart in (a) the camera image is rotated and the geographical longitude and latitude in the image is calculated for a height of 110 km. An overpass of the DMSP-16 is shown in white. Blue arrows indicate the direction of motion of DMSP-16. The red circle indicates the location of KHO.

parameters are used to study ionospheric conditions during auroral continuum events, if overpasses are available. The conjunction finder from Swarm-Aurora is used to check for possible overpasses of DMSP satellites [2]. Overpasses prior to or after auroral continuum events are also studied. Data from the satellites DMSP-15, DMSP-16, DMSP-17 and DMSP-18 is downloaded from the Madrigal Database at CEDAR [42].

In order to visualize a satellite overpass the images taken with the Sony A7s camera have to be calibrated to find the geographical longitude and latitude. A MATLAB script is used to overlay a camera image with a sky chart of 20 stars of which the position relative to KHO has been defined previously, as shown in Figure 3.6a cite. By finding the position of the stars in the camera image, the geographical longitude and latitude are calculated for a height of 110 km. Figure 3.6b shows the overpass of the DMSP-16 satellite on the calibrated image. From the overpass it is clear when the satellite performs measurements close to an auroral event.

3.5 NASA OMNIWeb data explorer

The OMNIWeb data explorer provides solar wind, magnetic field and plasma data from the ACE, Wind, IMP 8 and Geotail spacecraft in a one and five minute resolution [35]. The spacecraft have a stationary orbit close to the L1 Lagrange point, 1.5 million km from Earth. The data is time-shifted to Earth's bow shock nose, enabling a more accurate estimate at the time of auroral events. In this work this data is used to study solar wind, magnetic field and plasma conditions during auroral continuum events. A python script is used to pair OMNIWeb data with auroral events saved during spectrograph data processing - see GitHub.

Chapter 4

Results & Discussion

In this chapter the results of this work are elaborated and discussed, regurlarly referring to the theory outlined in chapter 2. The first section discusses the auroral continuum events detected with the procedures described in chapter 3. In the second section special attention is given to the time distribution of detected events and shadow height of solar illumination in the ionosphere. Data from OMNIWeb data explorer is used to investigate ionospheric and geomagnetic conditions surrounding continuum events. In the third section data from DMSP satellite overpasses is used to study local ionospheric conditions surrounding continuum events.

4.1 Auroral continuum events

In this section an overview is given of detected auroral continuum events. In subsection 4.1.1 the most interesting continuum events, so-called 'fat' continuum events, are described. 'Thin' continuum events and events without a clear spectrum are described in subsection 4.1.2. Subsection 4.1.3 describes events that spectrally resemble continuum emission but visually do not show the white or pinkish color.

4.1.1 Fat events

The definition 'fat' continuum event refers to the relatively large spatial structure of these auroral events and long lifetime on the scale of an hour. Recently, Partamies et al. have published a paper on two fat continuum events detected on 03-01-2020 and 11-02-2024 with MISS-1 [41]. These events were also detected in the analysis described in chapter 3 and are shown in Figure A.1a and Figure 4.1a, respectively. Here, we report the detection of another two fat continuum events. The first event has been used as example in chapter 3, a camera image of the event is shown in Figure 3.2, the spectral image taken with MISS-2 and detected spectra are shown in Figure 3.5. The second event was detected on 15-12-2021 with MISS-1 and is shown in Figure 4.1b.

All fat continuum events, except the event in Figure 4.1b, show a clear spectral enhancement between the detected and reference spectra characteristic for auroral continuum emission. Although a clear spectral enhancement is absent in Figure 4.1b, it is believed that the event is indeed a continuum event as it shows the same dynamic behavior and spatial structure as the other events. It is interesting to note that the event in Figure 4.1b was not directly detected in the analysis. The code used for processing the data detected the observed red sky enigma instead [32]. After going through Sony camera images the fat continuum event was found. This raises the question how many more fat continuum events are present in the data but are obscured by e.g. airglow or clouds.

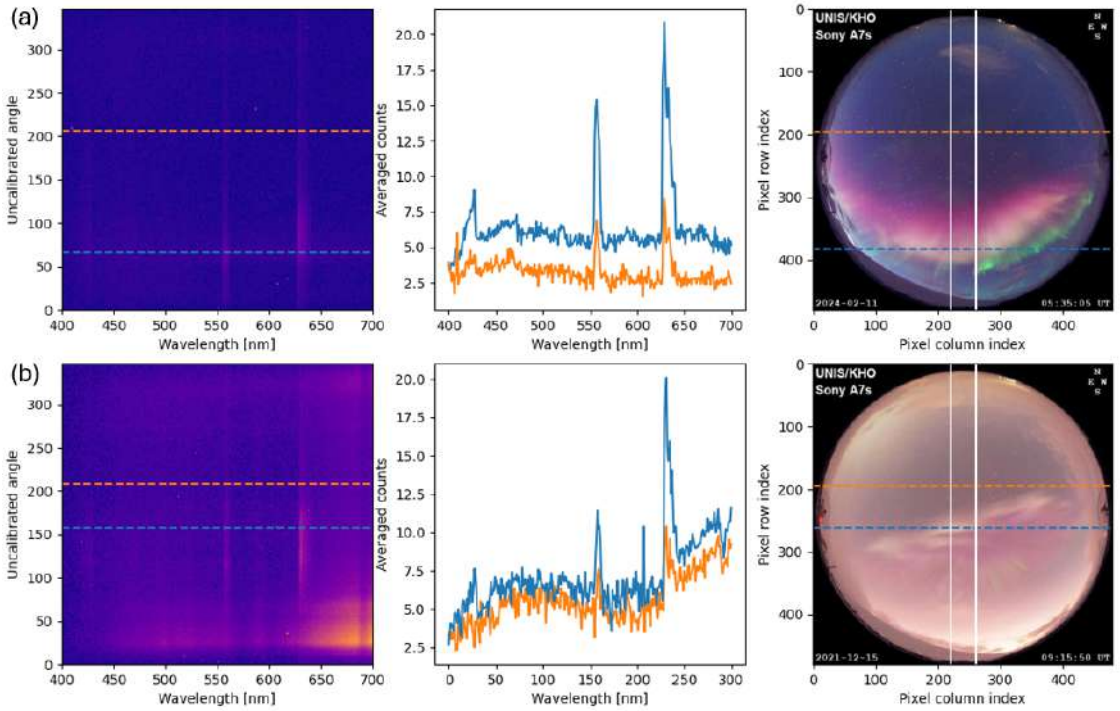

Figure 4.1: MISS-1 spectral image, averaged detected and reference spectra and Sony A7s camera image for the auroral fat continuum events on (a) 11-02-2024 and (b) 15-12-2021. Spectral images are taken at (a) 05:35:00 UT and (b) 09:16:00 UT. Sony camera images are taken at (a) 05:35:05 UT and (b) 09:15:50 UT.

Continuum events of a smaller spatial structure and shorter lifetime on the scale of seconds to minutes, here referred to as 'thin' continuum events, have been reported by Partamies et al. and Spanswick et al. [41, 46] and are also observed in this work.

4.1.2 Thin and possible events

Thin continuum events are detected in the data from MISS-1 and MISS-2. One thin continuum event detected with MISS-1 on 28-02-2020 is shown in Figure 4.2a. Another event, detected with MISS-2 on 01-02-2025, is shown in Figure 4.2b. Both events show a clear spectral enhancement between the detected and reference spectra over the full spectral range. The smaller spatial structure of these events, compared to the fat continuum events, is apparent from the Sony camera images. It is interesting that the event on 28-02-2020 is not embedded in a larger pink aurora, in contrast to the event on 01-02-2025 and fat continuum events highlighted in the previous section. This suggests that continuum events can occur in a variety of auroral precipitation conditions. The pink aurora, associated with the sunlit ionosphere, is discussed further in section 4.2.

The event observed on 28-02-2020 was also not directly detected in the analysis. Instead, the script detected the neighbouring intense green auroral event with emission from the first positive group of molecular nitrogen, similar to the events shown in Figure B.1. Only by visual inspection it was found that the thin continuum event is present. In this case the event is not directly detected because the blue auroral emission line is not visible in the spectral image, as shown in Figure 4.2a. This condition was already discarded for MISS-2, as described in section 3.2. It is advised to use a similar approach for MISS-1 data as more continuum events can be detected. This was not done in this work due to time constraints.

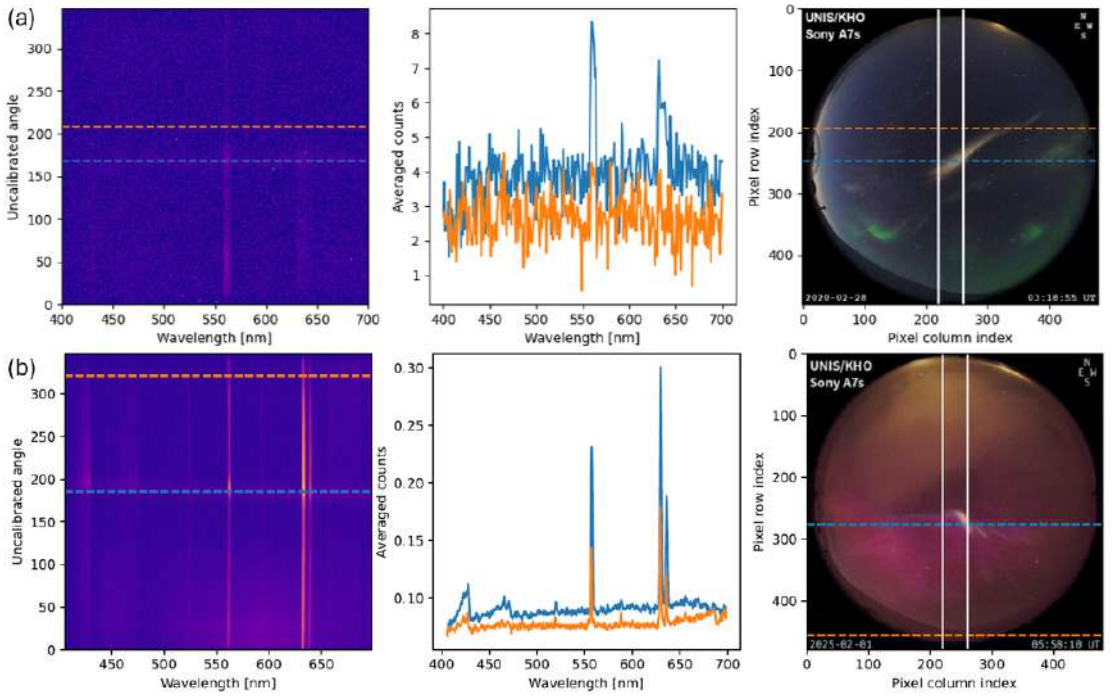

Figure 4.2: (a) MISS-1 and (b) MISS-2 spectral image, averaged detected and reference spectra and Sony A7s camera image for the auroral thin continuum events on (a) 28-02-2020 and (b) 01-22-2025. Spectral images are taken at (a) 03:19:00 UT and (b) 05:58:15 UT. Sony camera images are taken at (a) 03:18:55 UT and (b) 05:58:10 UT.

More possible thin continuum events have been indirectly recognized in the data. Appendix B shows a list of all events with corresponding Sony A7s camera images. Spectral images are not available for these events, either due to the events being too faint or not crossing the meridian where the spectrographs are pointed at. It is interesting that the events are either embedded in a larger pink auroral structure, see Figure B.2, or are observed next to a green auroral event with emission from the first positive group of molecular nitrogen, see Figure B.1. Again, the sunlit ionosphere is further discussed in section 4.2.

4.1.3 Fake continuum events

Care should be taken with the events listed in Appendix B. Due to absence of spectral images it is not possible to determine a spectral enhancement and conclude whether the events are real continuum events. There are reports from the observatory in Skibotn, Norway of auroral events that look white in color, but do not show a spectral enhancement. Conversely, in this analysis we have also identified events that show a spectral enhancement over the full spectral range but no apparent white or pinkish color associated with continuum emission. Several of such possibly 'fake' continuum events are shown in Appendix B.2.

4.2 Continuum emission in the sunlit ionosphere

The goal of this work is to investigate the conditions under which continuum events occur to understand the origin of auroral continuum emission. In this section we first investigate the pink aurora that is associated with the sunlit ionosphere and is observed for all fat continuum events and several thin continuum events. Then, in subsection 4.2.2, we investigate auroral precipitation and ionospheric activity measured during the fat continuum events and compare it to events in similar sunlit conditions. Finally, in subsection 4.2.3 we use the knowledge gained in this section to search for additional fat continuum events in Sony A7s camera data based on the solar wind and ionospheric conditions they are observed in.

4.2.1 Shadow height distribution of continuum events

It is known that pink aurora in the dayside auroral oval is caused by the upwelling of nitrogen (ions) and consequent fluorenscence in the sunlit ionosphere, described in section. It is interesting that all fat continuum events are observed in these conditions. It has been suggested that N_2, when heated by particle precipitation or plasma flow in the ionosphere, could be the origin of continuum emission by forming NO_2, similar to STEVE [41, 46, 20].

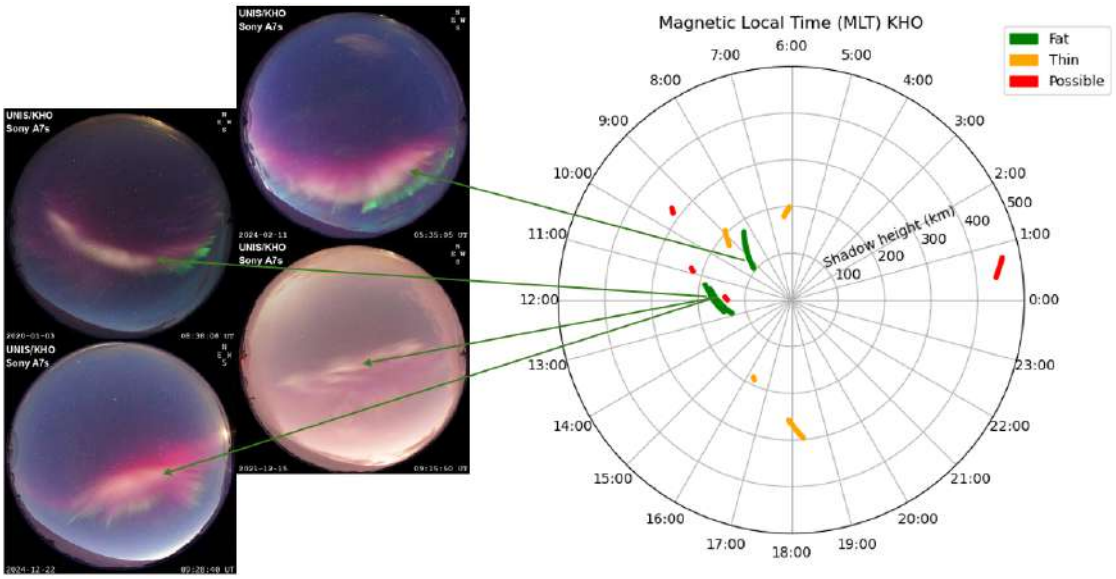

Figure 4.3: The time distribution of detected auroral continuum events as estimated from the Sony A7s camera. The angular axis is in magnetic local time (UT + 2.5) at the Kjell Henriksen Observatory (KHO). The radial axis is the shadow height of solar illumination in the ionosphere above KHO. The legend classifies the events into the categories defined in this report. Images of fat continuum events are added on the left.

In Figure 4.3 we consider the shadow height of solar illumination in the ionosphere during detected continuum events. The angular axis is in magnetic local time (MLT) at KHO, which is UT + 2.5 hours. The start and end time of the events has been determined from the first white or pinkish emission visible with the Sony A7s camera until it has disappeared. The radial axis is the shadow height, determined with a MATLAB script cite. The events in Figure B.2a,d have been added to the 'thin' category in this plot due to their convincing spatial structure. The most striking observation in Figure 4.3 is that three out of four known fat continuum events are all observed around magnetic noon between 100 - 200 km shadow height. The fourth event is also observed at a shadow height of 100 - 200 km but earlier in the morning around 09:00 MLT.

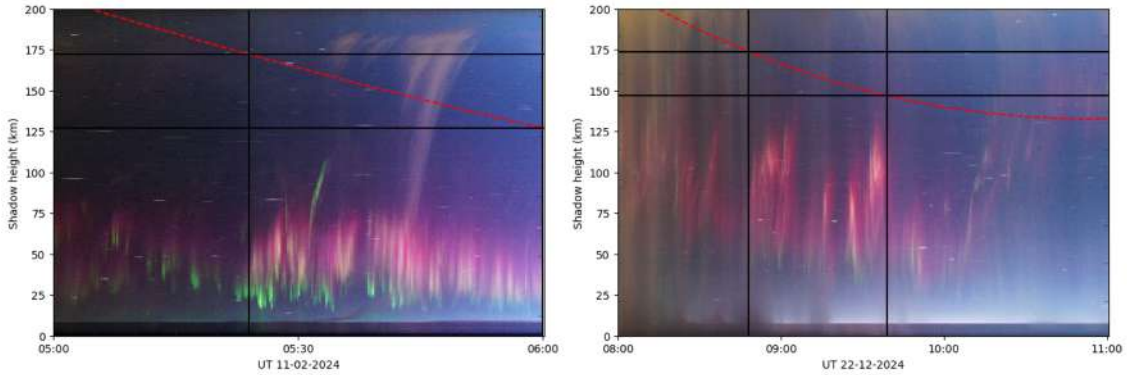

Figure 4.4: Keograms from high resolution Sony A7s camera images for the fat continuum events on (left) 11-02-2024 and (right) 22-12-2024. The red dashed line shows the evolution of the shadow height in the ionosphere above KHO as a function of time. The black lines indicate the interval during which the fat continuum events are observed. The y-axis is not scaled to the keogram but to the red dashed line.

For a more accurate analysis, Figure 4.4 shows high resolution keograms of the auroral continuum events on 11-02-2024 and 22-12-2024 together with the derived shadow height. The y-axis is not scaled to the keogram but to the red dashed line showing the evolution of the shadow height as a function of time. The black lines indicate the interval during which the event is observed. The events on 11-02-2024 and 22-12-2024 begin at a shadow height of 172 and 173 km, respectively, and end at a shadow height of 127 and 147 km, respectively. Keograms of the other two fat continuum events are shown in Appendix C and occur for similar shadow heights.

A recent suggestion states that continuum emission is not caused by the formation of NO_2 but is Vegard-Kaplan band emission from N_2+ ions. The observed shadow heights are consistent with favorable conditions for N_2+ ions in the sunlit ionosphere. In general, it is known that ion upflow in the dayside aurora is paired with enhanced electron- and ion temperatures [28]. Furthermore, it has been derived that in the sunlit ionosphere over Svalbard, the lifetime of N_2+ increases from an order of milliseconds at 100 km altitude to seconds at 200 km altitude [30]. A peak in the N_2+ density on the order of 10^3 ions/cm^3 has been recorded around a shadow height of 150 km - see Figure 2.7b [25]. Below 150 km the penetration depth of solar radiation drops and charge-transfer interactions with oxygen increase [10, 25]. High rotational temperatures of N_2+ ions above 1000 K have been recorded at shadow heights around 150 km [30]. With a high rotational temperature, the emission lines of the Vegard-Kaplan band could be broadened to the point that they overlap and form a continuum spectrum [7].

4.2.2 Ionospheric conditions surrounding continuum events

Pink aurora is observed frequently in the dayside auroral oval, but not always associated with continuum emission. It is possible that additional sources of energy, such as strong particle precipitation or ionospheric convection, are required to produce continuum emission. In this section we investigate solar wind and ionospheric activity surrounding fat continuum events with data from the OMNIWeb data explorer [35].

In order to draw valid conclusions we require a collection of events with pink aurora in similar sunlit conditions as the fat continuum events. Knowing that the fat continuum events are observed around a shadow height of 150 km, the time when this shadow height is reached is calculated for each day that the Sony A7s camera has recorded. From the images the events

with visible pink aurora are selected. Days during the midnight sun, when the shadow height is always below 150 km, are excluded. The Sony A7s camera has been operational since 2015. After removing clouds, clear skies and green aurora, 135 events with pink aurora and a shadow height of 150 km are obtained.

OMNIWeb data is downloaded as 5 min averaged and analyzed with self-defined python functions cite. We start with discussing the auroral electrojet (AE) index, shown in Figure 4.5a, for all pink aurora events (blue) and three of the fat continuum events detected in the previous sections with the MISS spectrographs (orange). There is no value for the continuum event on 03-01-2020 at the instance the shadow height reaches 150 km. (Spoiler alert) The fat continuum events shown in red are discussed in the next section. The black dashed line indicates the average value of all events.

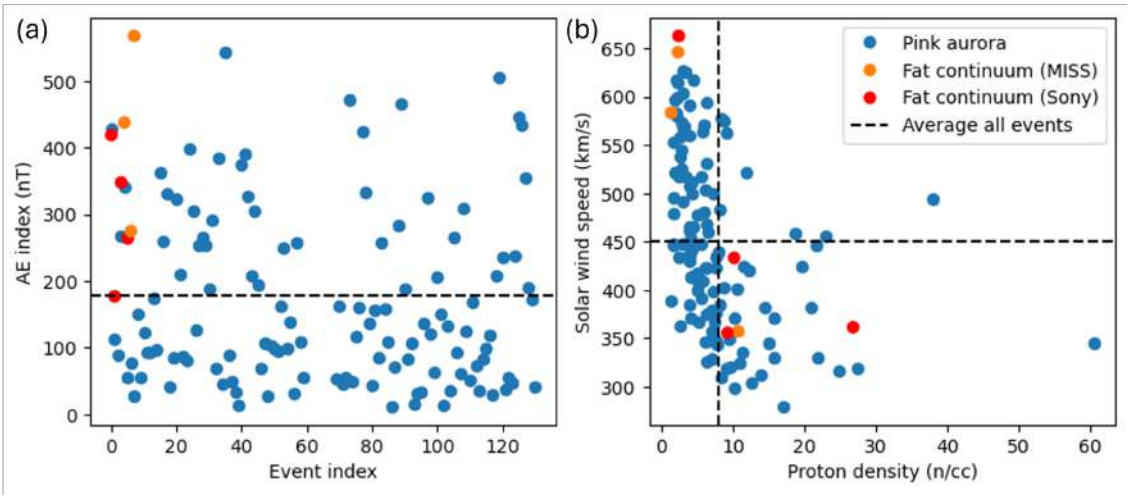

Figure 4.5: (a) Auroral electrojet (AE) index for all pink aurora events and fat continuum events. The dashed line indicates the average value of all events. Legend shown in (b). (b) Solar wind speed against proton density for the same events as in (a). The measured solar wind speed and proton density is time-shifted to Earth's bow shock, all data is 5 min averaged, downloaded from OMNIWeb [35].

The AE index is a measure for the strength of the auroral electrojets, described in section 2.1.3. Figure 4.5a shows that the AE index for the known fat continuum events (orange) is 100 - 400 nT higher than the average value. This is consistent with observations with the Sony A7s camera, all four fat continuum events show an eastward motion across the sky, corresponding with eastward convection in the westward electrojet - see section 2.1.3. The correlation of fat continuum events with an enhanced auroral electrojet is interesting beause a similar mechanism is suggested for STEVE, where subauroral ion drifts (SAIDs) are associated with the formation of NO_2 [20]. STEVE requires a minimum velocity of 4.4 km/s for NO+ ions in SAIDs to excite nitrogen molecules to a higher vibrational state and form NO_2 [20]. Vertical and horizontal plasma velocities and energy fluxes during fat continuum events are investigated in section 4.3 with DMSP satellite overpasses. Considering Vegard-Kaplan band emission from N_2+ ions, the auroral electrojet could be a source of additional rotational energy for N_2+ ions in the form of collisions between moving plasma and neutrals, broadening the emission lines.

In Figure 4.5b the solar wind speed is plotted against the proton density. Data is missing from the fat continuum event on 15-12-2021. The figure shows that the fat continuum events (orange) occur either during a period of high solar wind speeds, above 550 km/s, or during a period of high proton densities, above 8 cm^{-3}. It is no surprise that high AE indeces are paired with high solar wind speeds or proton densities, as both are a likely driver of the au-

roral electrojet [3]. Furthermore, particle precipitation is one of the proposed mechanisms for generating ion upflow and heating the sunlit ionosphere [28]. In the sunlit ionosphere energetic particle precipitation is also a source of N_2+ ions through impact ionisation [10]. Sufficiently strong precipitation might provide the necessary conditions for continuum emission, either by Vegard-Kaplan band emission from N_2+ ions or by forming NO_2 [20].

4.2.3 Continuum event search based on ionospheric conditions

So far, the fat continuum events identified in section 4.1.1 from spectrograph data are the only known events of this category. In this section we have so far found that all fat continuum events are observed in the dayside auroral oval above Svalbard, characterized by a sunlit ionosphere that provides favorable conditions for the proposed sources of continuum emission. In Figure 4.5 ionospheric conditions surrounding fat continuum events are compared to events in similar sunlit conditions, which shows that fat continuum events are associated with enhanced auroral electrojet activity and particle precipitation. Knowing the conditions under which fat continuum events are observed provides the opportunity to perform a direct search for additional fat continuum events.

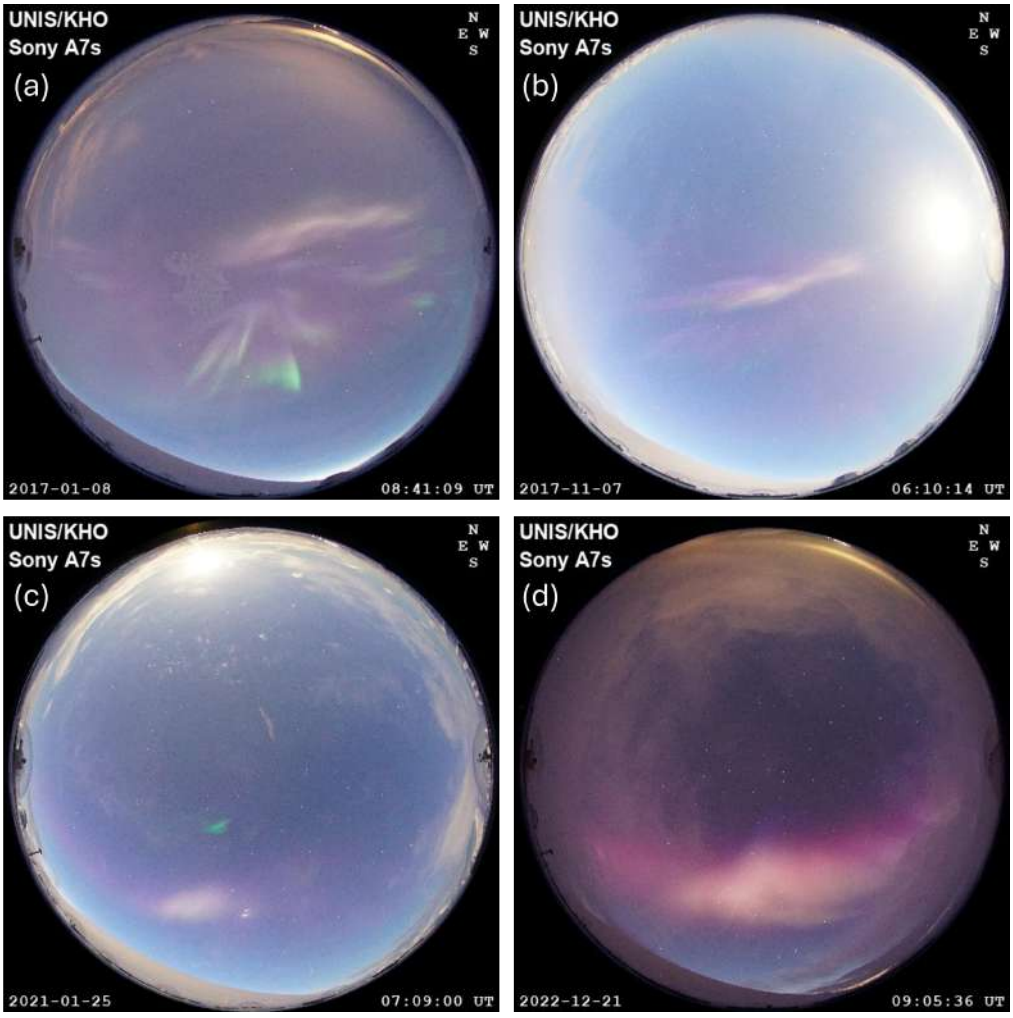

Figure 4.6: Fat continuum events identified in Sony A7s camera images on (a) 08-01-2017 at 08:41:09 UT, (b) 07-11-2017 at 06:10:14 UT, (c) 25-01-2021 at 07:09:00 UT and (d) 21-12-2022 at 09:05:36 UT based on the ionospheric conditions.

The Sony A7s camera has been operational since 2015, effectively 5 seasons longer than MISS-1 considering the complications during its first years of operation. Searching for fat continuum events in camera images is a logical next step now that we now the spatial and temporal characteristics of fat continuum events and know what days to investigate based on the ionospheric conditions. Based on the data in Figure 4.5, 20 pink aurora events with an AE index above 200 nT and solar wind speed above 550 km/s, or a proton density above 8 cm^{-3}, are considered. Additional images are used to create 30 min videos prior to the 150 km shadow height mark to visually investigate these events over a longer time period.

In the 20 events, three new fat continuum events are identified, shown in Figure 4.6a,c-d. Another fat continuum event is identified in the events with a high solar wind speed above 550 km/s or proton density above 8 cm^{-3}, but with an AE index below 200 nT, shown in Figure 4.6b. The AE index for this event is 177 nT as the shadow height reaches 150 km, but is 195 nT at the moment that the event is observed. The AE index, solar wind speed and proton density for these four newly identified fat continuum events are shown in Figure 4.5 in red. It is unknown whether fat continuum emission occurs during the other 17 days with a high AE index and particle precipitation. The solar wind and auroral electrojet affect the ionosphere globally, even if also the upwelling of nitrogen in the dayside aurora is required for continuum emission, it is possible that it occurs outside the view from KHO.

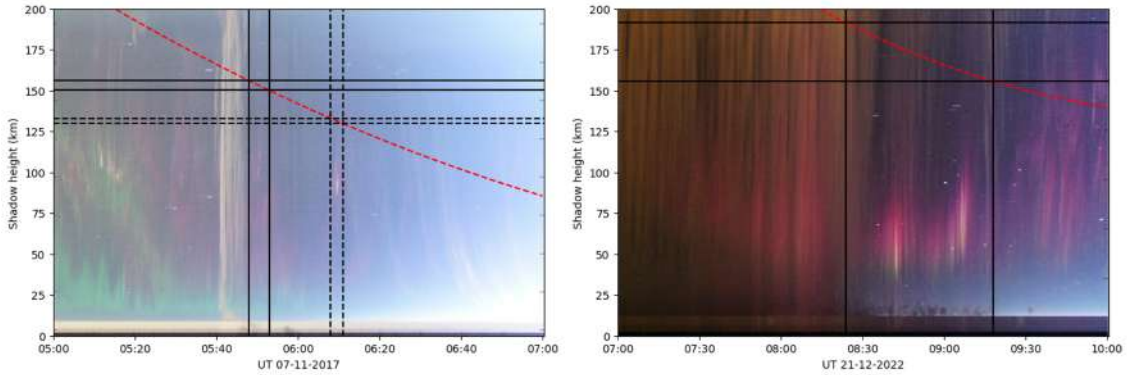

Figure 4.7: Keograms from high resolution Sony A7s camera images for the fat continuum events on (left) 07-11-2017 and (right) 21-12-2022. The red dashed line shows the evolution of the shadow height in the ionosphere above KHO as a function of time. The black lines indicate the interval during which the fat continuum events are observed. The y-axis is not scaled to the keogram but to the red dashed line.

The fact that the number of known fat continuum events doubles from this analysis is a strong indication that the magnitude of the auroral electrojet and particle precipitation are important factors for the occurence of continuum emission. Figure 4.7 shows keograms from the fat continuum events on 07-11-2017 and 21-12-2022, again overlayed with the derived shadow height as a function of time. Keograms of the other two new fat continuum events are shown in Appendix C. It is observed that all eight fat continuum events occur during a shadow height in the range of 120 - 200 km, which indicates also a strong correlation with the sunlit ionosphere.

4.2.4 Temporal evolution of ionospheric conditions

In this section we continue to investigate the correlation of continuum emission with the auroral electrojet by considering the dynamics of fat continuum events. Several fat continuum events, such as the events on 11-02-2024 and 21-12-2022, shown in Figure 4.4 and Figure 4.7, respectively, show a single period of continuum emission. Other fat continuum events, such as the events on 22-12-2024 and 07-11-2017, shown in the same figures, show several

periods of continuum emission with little auroral activity in between, which can last up to 20 minutes. It is investigated whether this corresponds with a change in the magnitude of the auroral electrojet.

Another interesting observation is the flow direction of the fat continuum events. All fat continuum events show fast eastward motion, except the event on 07-11-2017 which shows westward motion. To investigate this we explore the different components of the interplanetary magnetic field (IMF). It is known that the B_y component alters the dawn-dusk asymmetry in the ionospheric convection cells, described in section 2.1.3, and hence determines whether westward or eastward flow is observed around magnetic noon [22]. Furthermore, the magnitude and direction of the B_y and B_z component influence magnetic reconnection. Bursts of enhanced velocities in the auroral electrojet are observed in a number of aperiodic reconnection phenomena and flux transfer events [22, 33]. Bursts of enhanced velocities might explain why continuum emission is observed in periods of varying timescales rather than a single unbroken event, this is referred to as the 'bursty' nature of some fat continuum events for the remainder of this report.

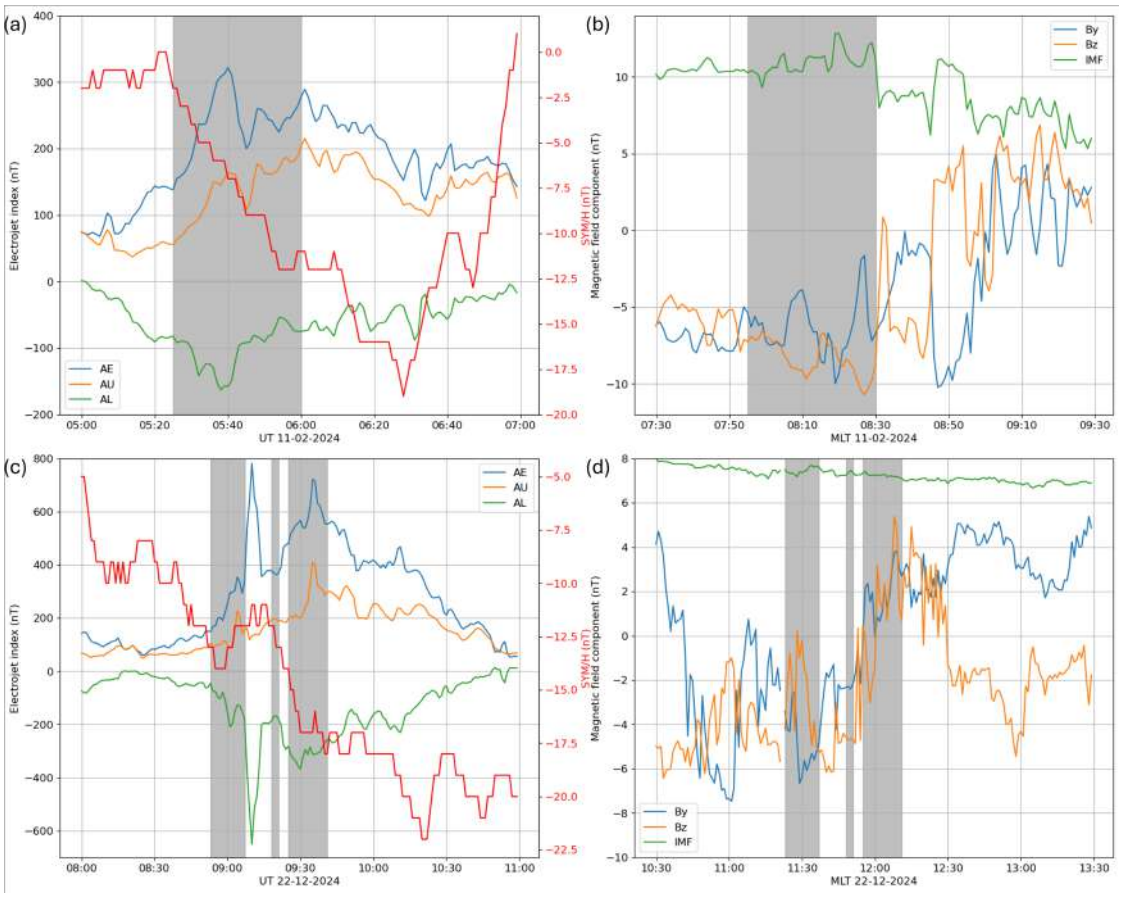

Figure 4.8: (a) The AE, AU, AL and SYM/H indeces as a function of time on 11-02-2024. (b) The By and Bz component of the IMF as well as the total IMF magnitude as a function of magnetic local time (UT+2.5) on 11-02-2024, the same period as (a). (c) The same as (a) but on 22-12-2024. (d) Same as (c) but on 22-12-2024 with the same period as (c). Grey shaded areas highlight the observation of fat continuum emission. All data is 1 min averaged and magnetic field values are time-shifted to Earth's bow shock, from OMNIWeb [35].

Figure 4.8a,c and Figure 4.9a,c show the AE, AU, AL and SYM/H indeces as a function of time for the four fat continuum events shown in the keograms in Figure 4.4 and Figure 4.7,

respectively. The same period of time as shown in the keograms is used, except for the event on 11-02-2024 where an additional hour is added in Figure 4.8a. Figure 4.8b,d and Figure 4.9b,d show the B_y and B_z IMF component as well as the total IMF magnitude for the same events in the same period of time, now defined in magnetic local time (UT + 2.5). The grey shaded areas highlight the periods when continuum emission is observed. Similar figures are created for the remaining four fat continuum events and shown in Appendix C alongside the respective keograms.

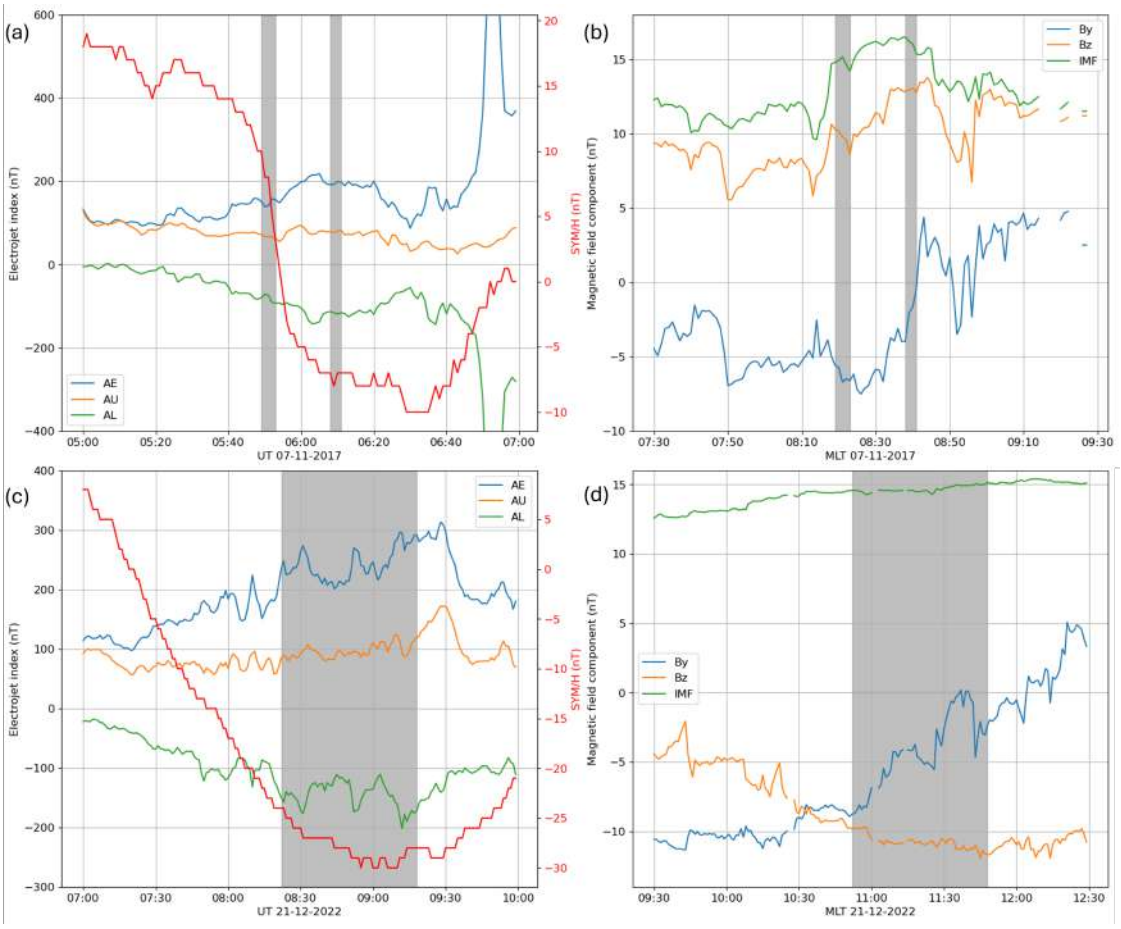

Figure 4.9: (a) The AE, AU, AL and SYM/H indeces as a function of time on 07-11-2017. (b) The By and Bz component of the IMF as well as the total IMF magnitude as a function of magnetic local time (UT+2.5) on 07-11-2017, the same period as (a). (c) The same as (a) but on 21-12-2022. (d) Same as (c) but on 21-12-2022 with the same period as (c). Grey shaded areas highlight the observation of fat continuum emission. All data is 1 min averaged and magnetic field values are time-shifted to Earth's bow shock, from OMNIWeb [35].

The electrojet- and SYM/H indeces show a similar behavior for all fat continuum events. Continuum emission is observed as the SYM/H index declines. The SYM/H index is a measure for the ring current magnitude and increases when a magnetic storm develops. A high IMF magnitude is measured during all fat continuum events, making the onset of a magnetic storm likely. During the main phase of a magnetic storm, as the SYM/H index declines, field-aligned currents that link the magnetotail current with the ionosphere are enhanced [17]. As a result, hot particles from the magnetotail are channelled into the ionosphere. This is reflected by a simultaneous decline of the AL index. The AL index corresponds with the westward electrojet that encompasses the inflow along field-aligned currents from the

nightside, see section 2.1.2. Continuum emission is observed as the AL index approaches -100 nT or is already far below -100 nT, indicating a possible threshold value for the required magnitude of ionospheric convection.

According to literature, the observed eastward flow direction of fat continuum events is expected in the magnetic (pre)-noon sector in the westward electrojet for a strong negative B_z and B_y component, where most events are observed [22]. The fat continuum event on 07-11-2017 flows westward, even though it occurs in the magnetic morning sector and with a strong negative B_y component. The event on 07-11-2017 is also the only fat continuum event that occurs during a strong nortward (positive) B_z component. The observed westward flow and strong northward B_z agree with the rare occurence of reverse cell convection in the ionosphere, aided by the northward B_z (NBZ) current in the cusp region [17, 48, 8]. Following this reasoning it is implied that fat continuum events occur in the F-region of the ionosphere where ions flow along the $E \times B$ direction, which would align with a shadow height around 150 km and upflow of particles into this eastward ion flow, however, the altitude of continuum emission has not yet been determined and is open for future research.

The development of a magnetic storm, paired with enhanced ionospheric convection and particle precipitation are likely the required conditions for fat continuum events to emerge. Yet, from the figures above it is clear that continuum emisison is not observed over the full time period of enhanced ionospheric convection but comes in 'bursts'. In the dayside aurora, below the cusp, aperiodic changes in the magnetic reconnection result locally in high convection velocities above 1 km/s [22, 33]. Fluctuations of several nT are observed both for the B_z and B_y component for all fat continuum events, aperiodicically modifying reconnection. The interplay of magnetic reconnection and continuum emission in the dayside aurora is outside the scope of this work, but is proposed for future research.

Bursts of enhanced convection might also explain the consistent observation of aurora-like fragments poleward of continuum emission events, as shown in Figure 4.6c. Sufficient ionospheric convection could provide the heating or electric field required for ion cyclotron waves (EIC), predicted as the origin of aurora-like fragments [51]. A similar machanism is predicted for the aurora-like streaks observed next to STEVE [44].

4.3 DMSP satellite overpasses

Satellites in the Defense Meteorological Defense Program (DMSP) regularly pass over Svalbard in the morning hours, as introduced in section 3.4. This provides the opportunity to locally measure parameters such as plasma flow speeds, particle temperatures and energy fluxes. The satellites are limited in their spatial and temporal resolution, it is unlikely that continuum emission occurs at the exact moment a satellite is over Svalbard. Therefore, data from DMSP satellites is used to substantiate the observations made in the previous subsection on the general geomagnetic conditions in which fat continuum events occur and to provide additional information for future studies.

Satellite overpasses are available for most fat continuum events within a maximum of 10 - 20 minutes between the closest overpass and occurence of continuum emission and within the view of KHO. No such overpasses are available for the event on 15-12-2021 and 11-02-2024. Most overpasses are moved to Appendix to ensure a concise discussion. In this section we discuss the overpasses for the fat continuum event on 03-01-2020. The overpasses in Appendix come to similar conclusions.

4.3.1 Satellite overpasses on 03-01-2020

The overpass of DMSP-17 on 03-01-2020, shown in Figure 4.10a, is the closest overpass to a fat continuum event available, spatially and temporally. Another overpass is available on 03-01-2020, this time by DMSP-15, and is shown in Figure 4.10b. DMSP-15 is further north than DMSP-17 with respect to the location of continuum emission, but does cross the auroral oval earlier outside the image. In the DMSP data, parameters are regularly measured with respect to either the direction of the satellite or the direction towards the sun. In Figures 4.10a,b the direction of the satellites is marked with blue arrows, the direction towards the sun is indicated by yellow arrows.

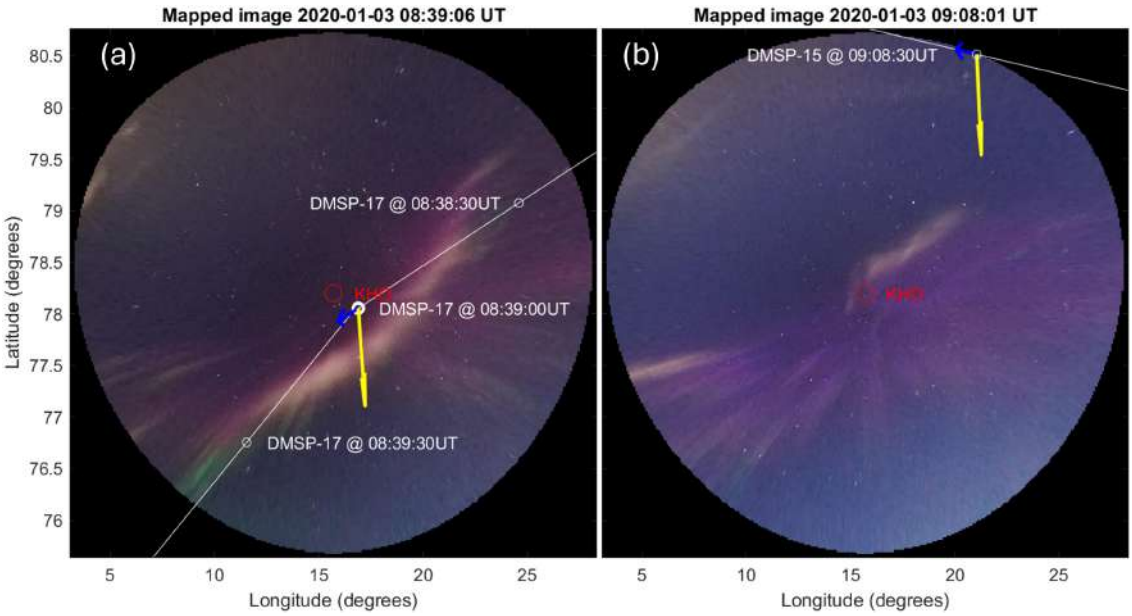

Figure 4.10: (a) Overpass trajectory DMSP-17 overlayed on Sony A7s camera image from 03-01-2020 at 08:39:06 UT. (b) Overpass trajectory DMSP-15 overlayed on Sony A7s camera image from 03-01-2020 at 09:08:01 UT. Blue arrows indicate the direction of the satellite. Yellow arrows indicate the vector towards the sun. The geographical location of KHO is shown in both (a) and (b).

4.3.2 Integrated energy fluxes

In the previous section it was found that all fat continuum events occur during the main phase of magnetic substorms, which is correlated with additional high energy particles entering the ionosphere along field-aligned currents (FACs) from the magnetotail. This results in higher auroral electrojet activity. A measure for the energy entering the ionosphere is given by the integrated energy flux. DMSP satellites measure the energy flux for particles with an energy in the range of 30 eV - 30 keV. The integrated energy flux is an average over the 19 measurement channels in this range.

Figure 4.11 shows the integrated energy flux of ions and electrons for the overpass of DMSP-17 on 03-01-2020. This data is not available for DMSP-15. Close to the continuum event at 08:39 UT, a flux of roughly 10^{10} eV/(cm^2·s·sr) is observed for both electrons and ions. Two higher peaks above 10^{11} eV/(cm^2·s·sr) are observed around a magnetic latitude of 70°. Xiong et al. have used DMSP satellites to investigate the relation between FACs in the ionosphere and particle precipitation under different conditions for B_z and B_y [52]. Energy fluxes around 10^{11} eV/(cm^2·s·sr) agree with measurements by Xiong et al. for B_z between 0 and -5 nT and B_y

between -5 and -10 nT, as determined for this fat continuum event in Figure C.2a. An energy flux around 10^{10} eV/(cm^2·s·sr) is in line with the cusp region where precipitating particles have less energy.

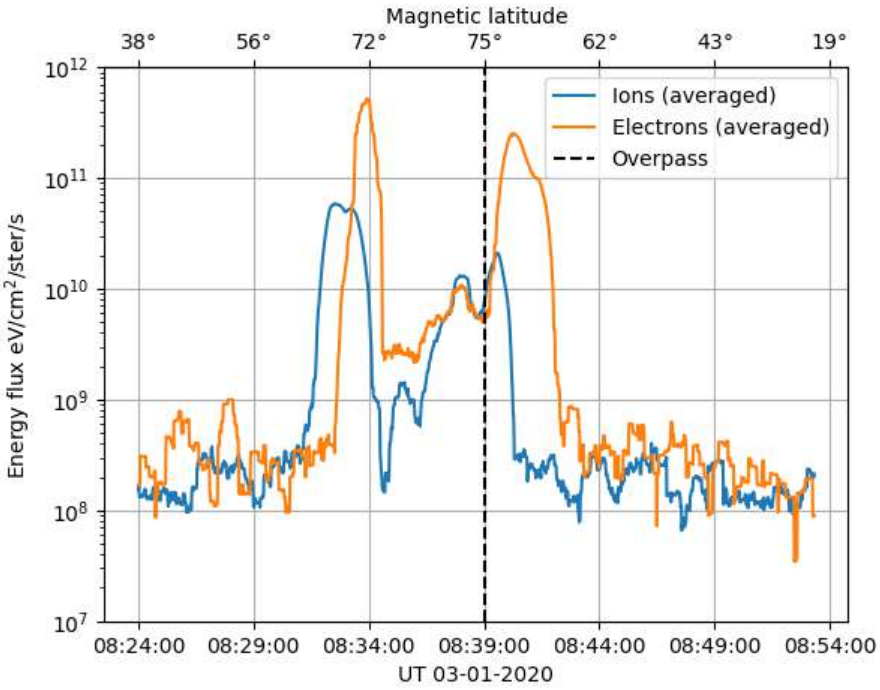

Figure 4.11: The integrated energy flux of ions and electrons in eV/cm^2/ster/s as a function of time (UT) and magnetic latitude for the overpass of the DMSP-17 satellite on 03-01-2020. The overpass at 08:39 UT is highlighted with a black dashed line.

In further studies, the integrated energy flux can be used to model the behavior of the auroral electrojet during fat continuum events. Furthermore, the energy deposited in the cusp region during the specific conditions for B_z and B_y can be used to model the influence of particle precipitation on the different proposed sources of continuum emission.

4.3.3 Differential energy flux spectrogram

In Figure 4.12 the energy flux of electrons is shown as measured by DMSP-17 for each of the 19 measurement channels, the differential energy flux. By considering each channel independently we create a spectrogram that highlights the dominant energy of incoming particles. Around 08:34 UT in Figure 4.12 a broad spectrum of electron energies is measured with most prominent an energy flux on the order of 10^9 eV/(cm^2·s·sr·ΔeV) for electrons with an energy approaching 1 keV. A broad electron spectrum is distinctive of the cusp boundary with open field lines [4]. Then, around 08:39 UT, a similar energy flux is measured for electrons with energies around 100 eV. Low energy electron precipitation on the order of 100 eV is expected within the cusp region, as described in section 2.2 and measured by Cai et al. [4]. Knowing the energy of electrons precipitating over continuum emission is important for future modelling efforts. After 08:39 UT there is a sharp increase to electron energies above 1 keV, reaching electron energies of 10 keV. It is expected that the satellite reaches a boundary of the cusp with closed field lines along which electrons are accelerated.

In Figure 4.13 we consider the ion energy flux as well as horizontal magnetic field disturbances measured by DMSP-17. Disturbances along the satellite trajectory and in the direction of the sun are shown in blue and purple, respectively. The horizontal black dashed line

indicates zero magnetic disturbance. Just before 08:34 UT an energy flux on the order of 10^7 eV/(cm^2·s·sr·ΔeV) is observed for energies around 10 keV. At the same time, an overall negative disturbance in the horizontal magnetic field components is measured. In the future this could be used to determine field-aligned current magnitudes and whether upflow or precipitation is expected [4, 52]. Ion energies of 10 keV correspond to regions inside the auroral oval but outside the cusp region. Around the overpass at 08:39 UT ions of lower energy around 1 keV are measured, but with an energy flux peaking to 10^8 eV/(cm^2·s·sr·ΔeV). These energies are in line with expectations for the cusp region [4]. Knowing the specific energy of ions in the cusp region is also important for future modelling of continuum emission. After 08:39 UT there is a positive peak in the magnetic field disturbances, indicating another field-aligned current but with opposite direction.

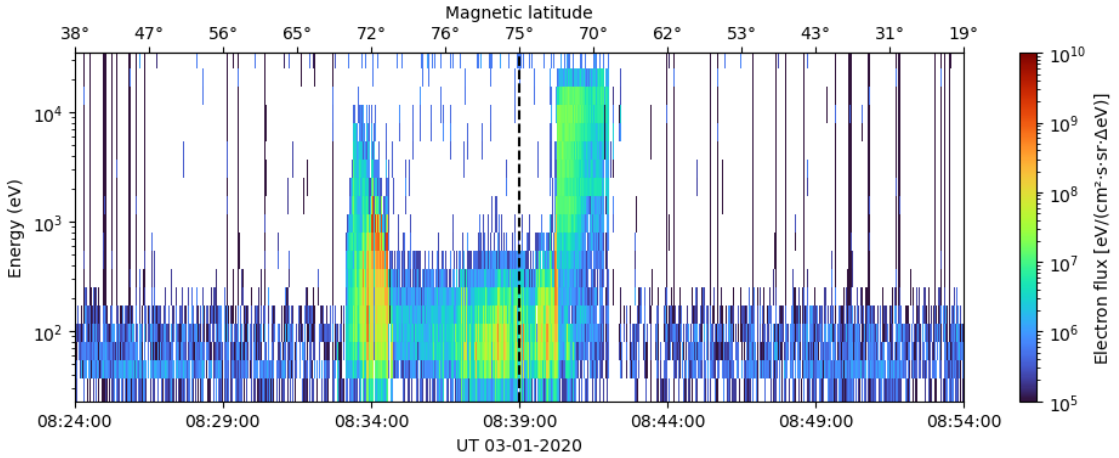

Figure 4.12: Electron energy fluxes measured in the 19 individual channels of DMSP-17 in the energy range of 30 eV - 30 keV as a function of time (UT) and magnetic latitude on 03-01-2020. The vertical black dashed line indicates the overpass at 08:39 UT.

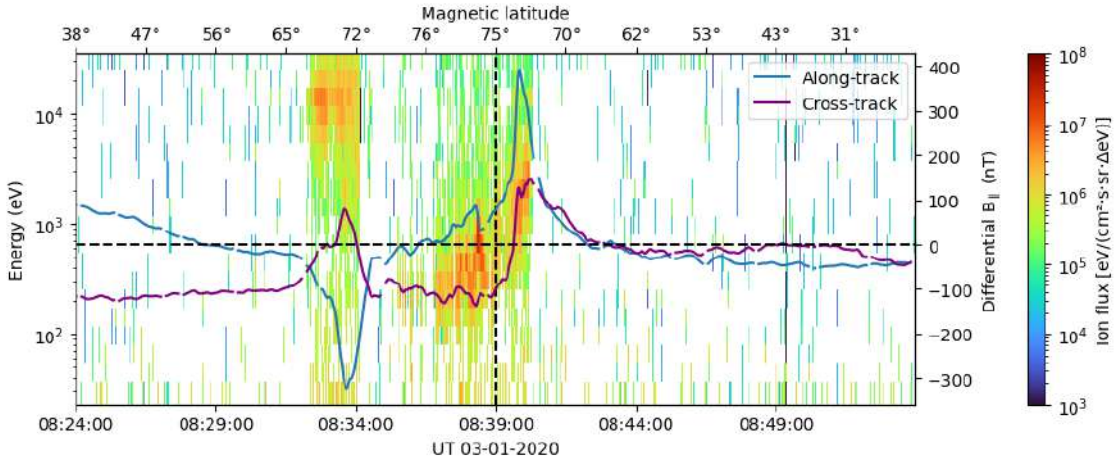

Figure 4.13: Ion energy fluxes measured in the 19 individual channels of DMSP-17 in the energy range of 30 eV - 30 keV as a function of time (UT) and magnetic latitude on 03-01-2020. The black dashed line indicates the overpass at 08:39 UT. Magnetic field disturbances measured along the track of the satellite (blue) and in the direction of the sun (cross-track,purple) are also shown. The horizontal black dashed line indicates zero magnetic field disturbance.

Considering the sunward trajectory of DMSP-17 and that the highest electron energies are measured past 08:39 UT, it is estimated that the edge of the cusp region is a couple of degrees south with respect to the continuum event. Defining the position of the cusp is important when considering aperiodic shifts in magnetic reconnection as a possible driver of continuum emission. It can be determined whether continuum events occur in the expected geographic location for reconnection phenomena by combining information on the plasma flow direction, cusp location and shifts in the IMF. Flow speeds in different directions can be determined from the magnetic field disturbances. This is outside the scope of this work.

4.3.4 Ion flow velocities

Vertical ion velocities (v_z) and horizontal ion velocities in the direction of the sun (v_y) measured by DMSP-17 and DMSP-15 are shown in Figures 4.14a,b. The black dashed lines again indicate the overpasses over Svalbard. High downward (positive v_z) ion velocities of roughly 4 km/s are observed at the overpass in Figure 4.14a. This data is noisy and likely not representative of the real situation. Upward ion velocities (negative v_z) are observed at the overpass in Figure 4.14b, north of the aurora and continuum emission visible in Figure 4.10. Upward ion velocities might indicate some unvisible extent of the cusp region in the ionosphere.

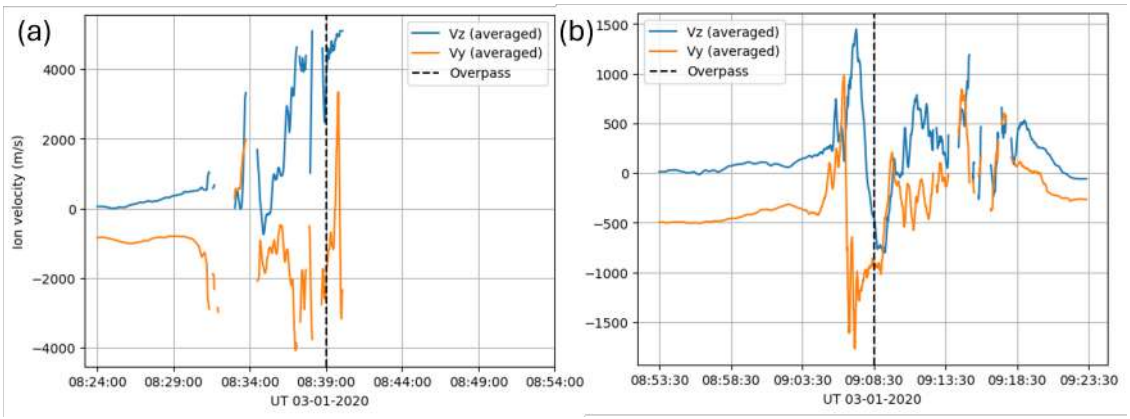

Figure 4.14: Vertical ion velocities (v_z) and horizontal ion velocities in the direction of the sun (v_y) measured by (a) DMSP-17 and (b) DMSP-15 on 03-01-2020. A positive v_z is defined as downflow of ions and positive v_y is defined as towards the sun. Black dashed lines indicate the overpasses over Svalbard.

The horizontal flow in Figures 4.14a,b is also noisy but has a reasonable magnitude when compared to measurements of high-latitude dayside aurora by Cai et al [4]. It is interesting that the cross-track velocity is anti-sunward. An anti-sunward velocity indicates that the flow is coming from the south where we estimated in the previous subsection the cusp edge to be located. Furthermore, an anti-sunward velocity aligns roughly with the observed motion of the continuum emission, although this is expected to occur at much lower altitudes. Further research is required to determine whether aperiodic reconnection phenomena flowing away from the reconnection point are responsible for continuum emission. In future research the SuperDARN or EISCAT radar could be used to investigate the nature of the observed 'bursts' in continuum emission as these radars provide a higher spatial and temporal resolution.

Chapter 5

Conclusion

In this work we have investigated ionospheric and geomagnetic conditions correlated with observations of auroral continuum emission in the dayside aurora over Svalbard. Initially, the number of known auroral continuum events is extended by designing the first version of a python script that automatically detects continuum events in the database of the MISS spectrographs located at the Kjell Henriksen Observatory - as described in chapter 3. Three types of continuum events are identified in section 4.1. Most prominent are so-called 'fat' continuum events - shown in section 4.1.1 - that can spatially extend over the full longitudinal range of the camera and persist on the timescale of an hour. Two additional fat continuum events are identified besides those investigated by Partamies et al. [41]. Several 'thin' continuum events - described in section 4.1.2 - with a smaller spatial structure and timescale on the order of seconds to minutes are also identified. Finally, possibly 'fake' continuum events are described in section 4.1.3. These events show a spectral enhancement in the full visible wavelength range, as expected for auroral continuum emission, but visually do not show the white or pinkish color associated with continuum emission. These events highlight the complications of identifying continuum emission with spectrographs. Sunlit conditions or reflections from clouds can easily obscure the spectrum of auroral events.

The fat continuum events are further investigated in this work. In section 4.2.1 it is shown that all four fat continuum events occur in the sunlit ionsphere for shadow heights between 100 - 200 km. In section 4.2.2 ionospheric conditions are investigated and compared to auroral events in similar sunlit conditions. It is observed that all four fat continuum events occur during a period of either high solar wind speeds (> 550 km/s) or high proton densities (> 8 n/cc) with a high AE index (> 200 nT). With this information, the Sony A7s camera is used to investigate auroral events in similar ionospheric conditions. In this procedure another four fat continuum events are identified that are not present in the database of the spectrographs - shown in section 4.2.3. The fact that the number of known fat continuum events doubles is a strong indication that the sunlit ionosphere, an enhanced auroral electrojet and particle precipitation are required conditions for the occurence of fat continuum emission.

In section 4.2.4 the temporal evolution of ionospheric and geomagnetic conditions is investigated and compared to the dynamic behavior of fat continuum events. It is observed that all eight fat continuum events occur during the main phase of a developing magnetic substorm. This aligns with an increase in the auroral electrojet magnitude. A possible treshold of -100 nT in the AL index is identified. Simultaneously, high IMF magnitudes and strongly negative B_z and B_y field components are measured for most events. A high IMF magnitude and/or particle precipitation are likely the driver of the magnetic substorm. A strong negative B_z ensures dayside magnetic reconnection and efficient transfer of energy into the sunlit ionosphere. A strong negative B_y component and the fact that all fat continuum

events occur during magnetic (pre)-noon aligns with the observed eastward motion of most fat continuum events. The event on 11-07-2017 shows westward motion, but is also the only event with a positive B_z component, likely causing reversed ionospheric convection. Aperiodic fluctuations are observed in the B_z and B_y component, which might indicate the occurence of aperiodic magnetic reconnection phenomena that could be correlated with the occurence of continuum emission, aurora-like fragments are observed regurlarly poleward of continuum emission.

Finally, DMSP satellite overpasses are highlighted in section 4.3 as a source of local measurements in the high altitude ionosphere. In section 4.3.2 it is shown that the measured integrated energy flux is in agreement with DMSP measurements in literature for similar magnitudes of the B_z and B_y component. In section 4.3.3 specific energy fluxes in the 30 eV - 30 keV energy range are investigated along with horizontal magnetic field disturbances. Single satellite measurements provide low resolution of the auroral oval, however, estimated ion energies align with literature and are used to possibly estimate the position of the cusp region relative to the observed continuum emission. Cross-track plasma flows measured by the satellite and inferred by the magnetic field disturbances align with the observed flow of continuum emisison.

In conclusion, this work has paved the way for further research on the origin of auroral continuum emission by significantly extending the list of known continuum events and identifying a correlation with specific ionospheric and geomagnetic conditions.

Chapter 6

Outlook

Possible further research and improvements on this specific work are plentiful. For this work specifically, the automated detection of auroral continuum events can be improved. As stated in chapter 3, two slightly different methods were used for the data from MISS-1 and MISS-2, mostly due to time constraints. It would be interesting to re-run the script on all MISS-1 data to see whether removing the condition to detect the blue auroral emission line results in the detection of additional continuum events. Furthermore, performing the row-wise mean in the same column range as MISS-2 might remove more false positives upfront by minimizing the influence of reflections from clouds or blue skies. For both MISS-1 and MISS-2 the peak detection functions can be optimized by performing a statistical analysis on a variety of auroral events to identify the optimal values for the minimum peak width and prominence to detect auroral emission lines. Detecting spectral enhancement in the row-wise mean could be improved by specifically considering the 480 - 520 nm range where little auroral emission is expected, however, spectra from clouds or blue skies are also prominent in this range. Based on this work, it could also be interesting to search specifically in the magnetic (pre)-noon sector for continuum events.

Then, future research following this work. It is strongly advised to start modelling the formation of NO_2 and Vegard-Kaplan band emission from N_2+ in the ionospheric conditions identified in this work. This work has provided a possible benchmark for the different sources of energy available during fat continuum events. From modelling it should become clear which thresholds, e.g. specific particle temperatures, plasma flow speeds or particle precipitation, should be reached to cause continuum emission and whether these are viable in the found ionospheric conditions.

Besides modelling, Fabry-Perot Interferometer (FPI) data was requested during this work to investigate whether also upflow of neutral nitrogen is present during the continuum events, which could indicate the production of NO_2. This data was not received and should still be investigated. Another important research question is at what altitude continuum emission occurs, this would show whether the events are in the auroral electrojet. It is also advised to investigate whether the Svalbard SuperDARN radar has identified flow speed channels related to aperiodic magnetic reconnection phenomena during some of the fat continuum events. Finally, the relation of magnetic reconnection, continuum emission and auroral-like fragments is an interesting option for further research.

There are some space missions that could provide novel information for this research as well. The EZIE cubesats have recently started gathering data on the structure and evolution of the auroral electrojets, which could be compared to the conditions of the electrojets during fat continuum events identified in this work [31]. Novel insights could also be obtained further in the future with the launch of the SMILE satellite.

Bibliography

[1] William Edward Archer, Bea Gallardo-Lacourt, Gareth William Perry, Jean-Pierre St.-Maurice, Stephan C Buchert, and Eric Donovan. Steve: The optical signature of intense subauroral ion drifts. *Geophysical Research Letters*, 46(12):6279–6286, 2019. 2

[2] University of Calgary Auroral Imaging Group. Swarm-aurora conjunction finder. https://swarm-aurora.com/conjunctionFinder/. [Accessed 15-05-2025]. 15

[3] Rolf Boström. A model of the auroral electrojets. *Journal of Geophysical Research (1896-1977)*, 69(23):4983–4999, 1964. 22

[4] L. Cai, A. Kullen, Y. Zhang, T. Karlsson, and A. Vaivads. Dmsp observations of high-latitude dayside aurora (hilda). *Journal of Geophysical Research: Space Physics*, 126(4):e2020JA028808, 2021. e2020JA028808 2020JA028808. 28, 29, 30

[5] I. J. Cohen, M. R. Lessard, R. H. Varney, K. Oksavik, M. Zettergren, and K. A. Lynch. Ion upflow dependence on ionospheric density and solar photoionization. *Journal of Geophysical Research: Space Physics*, 120(11):10039–10052, 2015. 8

[6] S. W. H. Cowley. *Excitation of Flow in the Earth's Magnetosphere-Ionosphere System: Observations by Incoherent-Scatter Radar*, pages 127–140. Springer Netherlands, Dordrecht, 1998. 6

[7] V. Degen. Synthetic spectra for auroral studies: The n2 vegard-kaplan band system. *Journal of Geophysical Research: Space Physics*, 87(A12):10541–10547, 1982. 20

[8] Yue Deng, Gang Lu, Young-Sil Kwak, Eric Sutton, Jeffrey Forbes, and Stan Solomon. Reversed ionospheric convections during the november 2004 storm: Impact on the upper atmosphere. *Journal of Geophysical Research: Space Physics*, 114(A7), 2009. 26

[9] R.H. Eather, S.B. Mende, and E.J. Weber. Dayside aurora and relevance to substorm current systems and dayside merging. *Journal of Geophysical Research: Space Physics*, 84(A7):3339–3359, 1979. 7

[10] P. G. Ellingsen, D. Lorentzen, D. Kenward, J. H. Hecht, J. S. Evans, F. Sigernes, and M. Lessard. Observations of sunlit n_2+ aurora at high altitudes during the renu2 flight. *Annales Geophysicae*, 39(5):849–859, 2021. 7, 8, 20, 22

[11] YI Feldstein, LI Gromova, A Grafe, C-I Meng, VV Kalegaev, II Alexeev, and Yu P Sumaruk. Auroral electrojet dynamics during magnetic storms, connection with plasma precipitation and large-scale structure of the magnetospheric magnetic field. In *Annales Geophysicae*, volume 17, pages 497–507. Springer, 1999. 6

[12] United Nations University Institute for Environment and Human Security. Space debris. https://interconnectedrisks.org/2023/tipping-points/space-debris. [Accessed 08-06-2025]. 1

[13] National Centers for Environmental Information NOAA. Defense meteorological satellite program (dmsp). https://www.ncei.noaa.gov/products/satellite/defense-meteorological-satellite-program. [Accessed 15-05-2025]. 14

[14] Harald U Frey, Desheng Han, Ryuho Kataoka, Marc R Lessard, Stephen E Milan, Yukitoshi Nishimura, Robert J Strangeway, and Ying Zou. Dayside aurora. *Space Science Reviews*, 215:1–32, 2019. 7

[15] With Qiang Fu. 4 - radiative transfer. In John M. Wallace and Peter V. Hobbs, editors, *Atmospheric Science (Second Edition)*, pages 113–152. Academic Press, San Diego, second edition edition, 2006. 8

[16] B. Gallardo-Lacourt, J. Liang, Y. Nishimura, and E. Donovan. On the origin of steve: Particle precipitation or ionospheric skyglow? *Geophysical Research Letters*, 45(16):7968–7973, 2018. 2

[17] N. Yu. Ganushkina, M. W. Liemohn, and S. Dubyagin. Current systems in the earth's magnetosphere. *Reviews of Geophysics*, 56(2):309–332, 2018. 5, 6, 25, 26

[18] D. M. Gillies, E. Donovan, D. Hampton, J. Liang, M. Connors, Y. Nishimura, B. Gallardo-Lacourt, and E. Spanswick. First observations from the trex spectrograph: The optical spectrum of steve and the picket fence phenomena. *Geophysical Research Letters*, 46(13):7207–7213, 2019. 2

[19] F. L. Guarnieri, B. T. Tsurutani, R. Hajra, E. Echer, and G. S. Lakhina. Norad tracking of the 2022 february starlink satellites and the immediate loss of 32 satellites. *Nonlinear Processes in Geophysics*, 32(1):75–88, 2025. 1

[20] Brian J. Harding, Stephen B. Mende, Colin C. Triplett, and Yen-Jung Joanne Wu. A mechanism for the steve continuum emission. *Geophysical Research Letters*, 47(7):e2020GL087102, 2020. e2020GL087102 2020GL087102. 2, 19, 21, 22

[21] Hiroshi Hasegawa. Magnetosphere continuously eats solar wind with a huge mouth. https://www.isas.jaxa.jp/en/feature/forefront/161226.html. [Accessed 12-06-2025]. 3

[22] K. Herlingshaw, L. J. Baddeley, K. Oksavik, and D. A. Lorentzen. A statistical study of polar cap flow channels and their imf by dependence. *Journal of Geophysical Research: Space Physics*, 125(11):e2020JA028359, 2020. e2020JA028359 10.1029/2020JA028359. 24, 26

[23] Katie Herlingshaw, Noora Partamies, Charlotte M. van Hazendonk, Mikko Syrjäsuo, Lisa J. Baddeley, Magnar G. Johnsen, Nina K. Eriksen, Ian McWhirter, Anasuya Aruliah, Mark J. Engebretson, Kjellmar Oksavik, Fred Sigernes, Dag A. Lorentzen, Takanori Nishiyama, Matthew B. Cooper, John Meriwether, Stein Haaland, and Daniel Whiter. Science highlights from the kjell henriksen observatory on svalbard. *Arctic Science*, 11:1–25, 2025. 7

[24] Katie Herlingshaw, Noora Partamies, Charlotte M. van Hazendonk, Mikko Syrjäsuo, Lisa J. Baddeley, Magnar G. Johnsen, Nina K. Eriksen, Ian McWhirter, Anasuya Aruliah, Mark J. Engebretson, Kjellmar Oksavik, Fred Sigernes, Dag A. Lorentzen, Takanori Nishiyama, Matthew B. Cooper, John Meriwether, Stein Haaland, and Daniel Whiter. Science highlights from the kjell henriksen observatory on svalbard. *Arctic Science*, 11:1–25, 2025. 9

[25] Donald M. Hunten. Sunlit aurora and the n2+ ion: a personal perspective. *Planetary and Space Science*, 51(13):887–890, 2003. 8, 20

[26] The University Centre in Svalbard. The meridian imaging svalbard spectrograph. https://aurora.unis.no/Instruments/MISS.html. [Accessed 12-05-2025]. 10

[27] The University Centre in Svalbard. Sony a7s all-sky camera. https://aurora.unis.no/Instruments/SonyA7s.html. [Accessed 13-05-2025]. 10

[28] Eun-Young Ji, Geonhwa Jee, and Changsup Lee. Characteristics of the occurrence of ion upflow in association with ion/electron heating in the polar ionosphere. *Journal of Geophysical Research: Space Physics*, 124(7):6226–6236, 2019. 7, 8, 20, 22

[29] Yong Ji, Lan Ma, Chao Shen, Gang Zeng, YanYan Yang, and Shuo Ti. Composite model for predicting sym-h index. *Earth and Space Science*, 10(10):e2022EA002560, 2023. e2022EA002560 2022EA002560. 6

[30] O. Jokiaho, B. S. Lanchester, and N. Ivchenko. Resonance scattering by auroral n_2^+: steady state theory and observations from svalbard. *Annales Geophysicae*, 27(9):3465–3478, 2009. 20

[31] John Hopkins Applied Physics Laboratory. Electrojet zeeman imaging explorer. https://ezie.jhuapl.edu/. [Accessed 04-06-2025]. 33

[32] N. D. Lloyd, D. A. Degenstein, F. Sigernes, E. J. Llewellyn, and D. A. Lorentzen. The red sky enigma over svalbard in december 2002: a model using polar stratospheric clouds. *Annales Geophysicae*, 23(5):1603–1610, 2005. 16

[33] G. Lu, S.W.H. Cowley, S.E. Milan, D.G. Sibeck, R.A. Greenwald, and T. Moretto. Solar wind effects on ionospheric convection: a review. *Journal of Atmospheric and Solar-Terrestrial Physics*, 64(2):145–157, 2002. STEP-Results, Applications and Modelling Phase (S-RAMP). 24, 26

[34] N. Martinez. The Meridian Imaging Svalbard Spectrograph 2: Enhancing Auroral Tracking Capacities. Master's thesis, Luleå University of Technology, 2024. 10

[35] Robert McGuire. Nasa omniweb data explorer. https://omniweb.gsfc.nasa.gov/html/hro_interface.html. [Accessed 15-05-2025]. 15, 20, 21, 24, 25, 46, 47

[36] Robert L. McPherron. The magnetopause current. https://www.britannica.com/science/geomagnetic-field/The-magnetopause-current. [Accessed 05-06-2025]. 4

[37] AB Meinel. The auroral spectrum from 6200 to 8900 a. *Astrophysical Journal, vol. 113, p. 583*, 113:583, 1951. 38

[38] Yukitoshi Nishimura, Alan Dyer, Lauri Kangas, Eric Donovan, and Vassilis Angelopoulos. Unsolved problems in strong thermal emission velocity enhancement (steve) and the picket fence. *Frontiers in Astronomy and Space Sciences*, Volume 10 - 2023, 2023. 1

[39] Fearghal O'Connor. Dozens of ryanair planes grounded after gps glitch hit multiple carriers worldwide. https://www.independent.ie/business/irish/dozens-of-ryanair-planes-grounded-after-gps-glitch-hit-multiple-carriers-worldwi
a1155320848.html. [Accessed 08-06-2025]. 1

[40] Macau Institute of Space Technology and Application. Space environment. https://mss.must.edu.mo/environment.html. [Accessed 05-06-2025]. 6

[41] N. Partamies, R. Dayton-Oxland, K. Herlingshaw, I. Virtanen, B. Gallardo-Lacourt, M. Syrjäsuo, F. Sigernes, T. Nishiyama, T. Nishimura, M. Barthelemy, A. Aruliah, D. Whiter, L. Mielke, M. Grandin, E. Karvinen, M. Spijkers, and V. Ledvina. First observations of continuum emission in dayside aurora. *EGUsphere*, 2024:1–28, 2024. 2, 16, 17, 19, 31, 43

[42] W. Rideout and K. Carigia. Cedar madrigal database. `http://cedar.openmadrigal.org`. [Accessed 15-05-2025]. 15

[43] H. Rishbeth. The ionospheric e-layer and f-layer dynamos — a tutorial review. *Journal of Atmospheric and Solar-Terrestrial Physics*, 59(15):1873–1880, 1997. 6

[44] Joshua Semeter, Michael Hunnekuhl, Elizabeth MacDonald, Michael Hirsch, Neil Zeller, Alexei Chernenkoff, and Jun Wang. The mysterious green streaks below steve. *AGU Advances*, 1(4):e2020AV000183, 2020. e2020AV000183 10.1029/2020AV000183. 26

[45] K. Shiokawa, Y. Otsuka, and M. Connors. Statistical study of auroral/resonant-scattering 427.8-nm emission observed at subauroral latitudes over 14 years. *Journal of Geophysical Research: Space Physics*, 124(11):9293–9301, 2019. 8

[46] E Spanswick, J Liang, J Houghton, D Chaddock, E Donovan, B Gallardo-Lacourt, C Keenan, J Rosehart, Y Nishimura, D Hampton, et al. Association of structured continuum emission with dynamic aurora. *Nature Communications*, 15(1):10802, 2024. 2, 17, 19, 38, 44

[47] Binod Sreenivasan. The earth's magnetic field and its dynamo origin. *Science and Culture*, 2018. 3

[48] T. Tanaka, T. Obara, M. Watanabe, S. Fujita, Y. Ebihara, R. Kataoka, and M. Den. Magnetosphere-ionosphere convection under the due northward imf. *Journal of Geophysical Research: Space Physics*, 124(8):6812–6832, 2019. 26

[49] Charlotte Van Camp and Walter Peeters. A world without satellite data as a result of a global cyber-attack. *Space Policy*, 59:101458, 2022. 1

[50] Aparna Venkatesan, James Lowenthal, Parvathy Prem, and Monica Vidaurri. The impact of satellite constellations on space as an ancestral global commons. *Nature Astronomy*, 4(11):1043–1048, 2020. 1

[51] D. K. Whiter, H. Sundberg, B. S. Lanchester, J. Dreyer, N. Partamies, N. Ivchenko, M. Z. Di Fraia, R. Oliver, A. Serpell-Stevens, T. Shaw-Diaz, and T. Braunersreuther. Fine-scale dynamics of fragmented aurora-like emissions. *Annales Geophysicae*, 39(6):975–989, 2021. 26

[52] Chao Xiong, Claudia Stolle, Patrick Alken, and Jan Rauberg. Relationship between large-scale ionospheric field-aligned currents and electron/ion precipitations: Dmsp observations. *Earth, Planets and Space*, 72:1–22, 2020. 27, 29

[53] TI Zvereva. Motion of the earth's magnetic poles in the last decade. *Geomagnetism and Aeronomy*, 52:261–269, 2012. 3

Appendix A

Spectrograph data processing

In this Appendix additional methods are elaborated that are used to organize or filter spectrograph data after initial data processing described in section 3.2. These methods are not essential to understand the results presented in chapter 4, but provide additional information to the python scripts available on GitHub and could aid further research on auroral continuum emission.

A.1 Different populations

After initial processing it is desired to organize the saved spectrograph data and search directly for auroral continuum events. It is expected that in the spectral range 480 - 520 nm there exist little emission from common auroral events, therefore, spectral enhancement in this range is a good indicator of continuum emission [46]. Figure A.1 shows the spectral image, detected and reference spectra and Sony A7s image of an auroral continuum event in (a) and common high intensity auroral event in (b). The continuum event has a relatively flat spectrum with a similar spectral enhancement over the full spectral range, with respect to the reference spectrum. For the event in (b) clear auroral peaks are visible besides the well-known green, blue and red emission lines. Note that for (b) there is indeed little emission between 480 - 520 nm. There is spectral enhancement between 650 - 700 nm, which is emission from the first positive group of molecular nitrogen seen for intense aurora [37].

Two populations are defined based on the spectra shown in Figure A.1. In Figure A.2 the spectral enhancement between 480 - 520 nm is shown in a scatter plot for all events saved for MISS-1 from the year 2020. Events are grouped and color coded for each unique day. The blue line is the ratio between the enhancement between 650 - 700 nm and 480 - 520 nm for each event. It is expected that continuum events as shown in Figure A.1a have a ratio close to 1 due to the relatively flat spectrum. Events with a higher ratio are expected to correspond to auroral events as shown in Figure A.1b which have spectral enhancement for 650 - 700 nm but not 480 - 520 nm. Figure A.2 shows that there are distinct groups of events that have a ratio close to 1 and a relatively high spectral enhancement between 480 - 520 nm compared to other events. A cut-off of ratio < 2 is chosen, indicated by the black dashed line in Figure A.2. Events with a ratio smaller than 2 belong to 'population 1' and events with ratio > 2 belong to 'population 2'. The same condition is used for MISS-2.

An advantage of this method is that population 2 consists mainly of intense auroral events that can be studied seperately if desired. A downside of this method is that sunlit and cloudy conditions also have spectral enhancement close to 480 - 520 nm. Thus, although seperated from intense auroral events, the false positives are mixed with continuum events. Additional filtering methods used for MISS-1 are described in the next section in this Appendix.

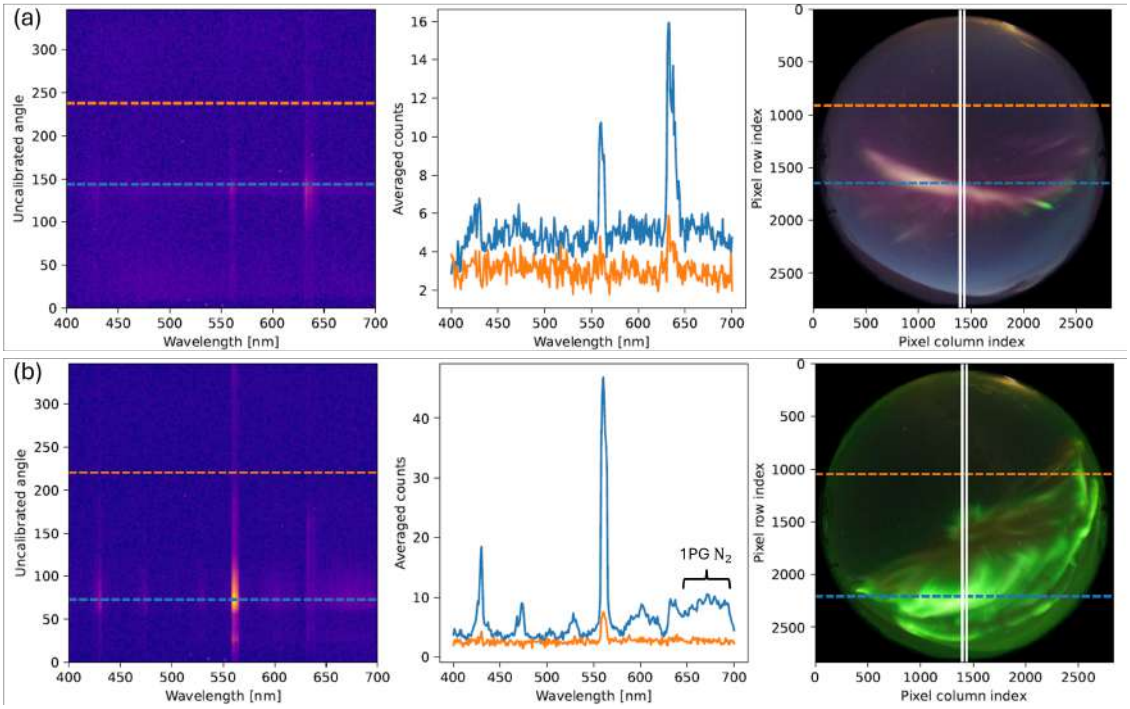

Figure A.1: (a) MISS-1 spectral image, averaged detected and reference spectra and Sony A7s camera image for the auroral continuum event on 03-01-2020 at 08:41 UT. (b) The same data as (a) for the auroral event on 02-01-2020 ar 23:18 UT. Emission from the first positive group of molecular nitrogen is highlighted.

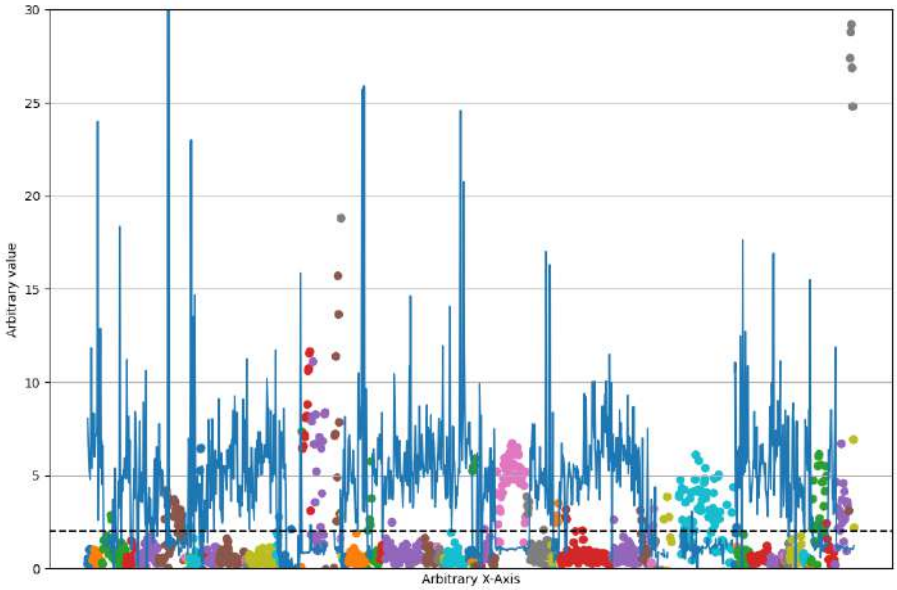

Figure A.2: The scatter plot shows the spectral enhancement in the 480-520 nm spectral range for all data saved for MISS-1 from the year 2020. The data is color grouped for each unique day. The blue line is the fraction between the spectral enhancement in the 650-700 and 480-520 nm spectral ranges for each event. The black dashed line indicates the cut-off value y=2.

A.2 Additional filtering methods MISS-1

Initial data processing on MISS-1 was conducted with an earlier version of the processing method compared to MISS-2, as described in section 3.2. Most notable is that the full spectral range is considered to detect peaks in the row-wise mean. It is expected that this procedure should be optimized to reduce the amount of false positives. Figure A.3 shows all 1761 events in population 1, as defined in the previous section, for MISS-1. Emission spectra with a large bulge around 460 nm are visible as well as some spectra that have a parabolic shape over the full spectral range. These spectra are from auroral events in dominating sunlit blue sky and/or cloudy conditions. The bulge around 460 nm or entire parabolic spectrum is picked up as a peak in the row-wise mean. Between roughly 560 - 640 nm these spectra are relatively flat, this range is considered to detect peaks in the row-wise mean for MISS-2.

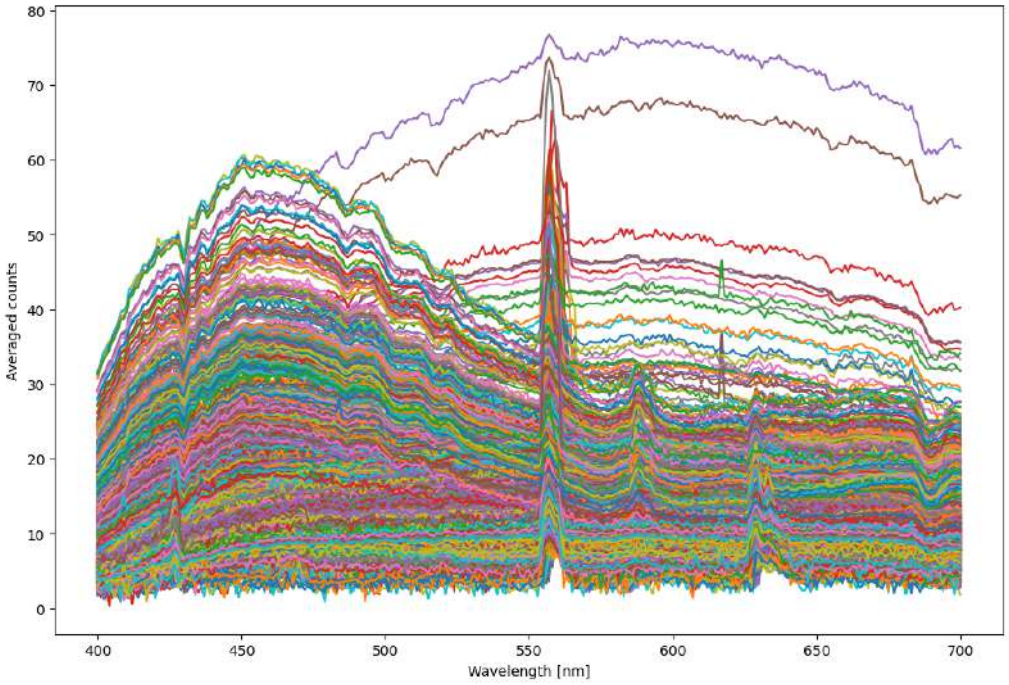

Figure A.3: The averaged detected spectra for all events in population 1 of MISS-1 plotted in averaged counts as a function of wavelength.

It is interesting that the false positives in Figure A.3 do not show the green, red and blue auroral emission line. Implying that an auroral event exists in the column-wise mean, but the sunlit spectrum is picked up in the row-wise mean. This can be exploited to filter out false positives. Similar to initial processing, the SciPy peak finding function is used to detect the red auroral emission line at 630.0 nm for the events in population 1. The full code is available on GitHub. With this method the amount of events is reduced from 1761 to 355, effectively filtering out false positives from sunlit or cloudy conditions.

Additionally, there is no condition that the spectral enhancement in the 480 - 520 nm range should be present. This was previously used in initial processing, but this was removed to keep initial processing simple and instead perform additional filtering. In this way a better understanding of the available data could be obtained. After filtering population 1 based on the red auroral emission line an additional condition is added that the spectral enhancement in the 480 - 520 nm range should be at least equal to 10%. This removes another 15 false positives. The remaining 340 events in population 1 are then filtered based on Sony A7s camera images, as described in section 3.3.

A.3 False positives MISS-2

Figure A.4 shows an example of the horizontal and slightly diagonal lines present in MISS-2 data for clear-sky conditions in (a) and cloudy conditions in (b). The horizontal lines are picked up during initial processing as peaks in the row-wise mean, resulting in false detection of possible continuum events. It is expected that the line in Figure A.4a is due to reflections from car lights shining at Breinosa mountain. The lines in Figure A.4b are likely due to reflections from the clouds, also seen for MISS-1 in the previous section. Removing reflections from clouds during initial processing is a difficult task. There is a variety of reflections from clouds of different intensity, besides the wide variety of auroral events that do have to be detected. It is advised to explore other methods to remove these reflections, for example by trying to fit a parabolic shape to the detected spectra or using meteorological data to filter out days with cloud-cover.

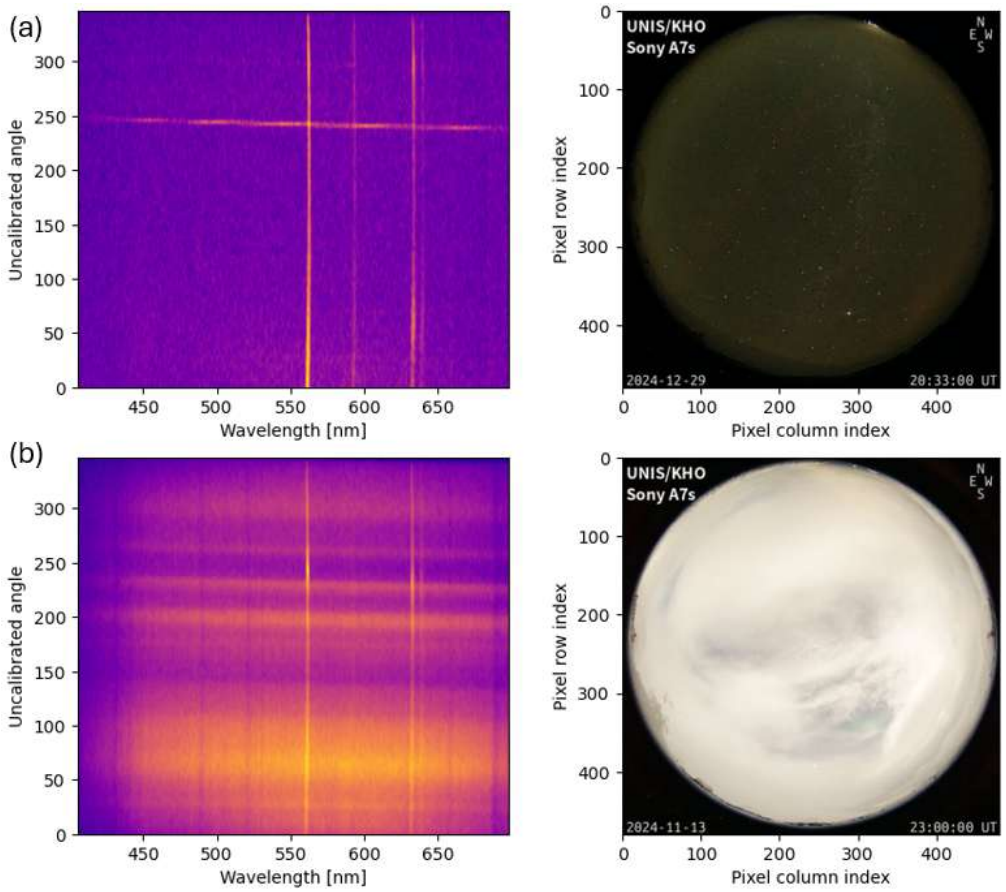

Figure A.4: Spectral image of MISS-2 and Sony A7s camera image captured at the same time on (a) 29-12-2024 at 20:33 UT and (b) 13-11-2024 at 23:00 UT. The spectral images show clear horizontal and slightly diagonal lines of higher intensity for (a) clear skies and (b) cloudy conditions.

Appendix B

Additional events

B.1 Possible continuum events

This section contains images of possible thin continuum events that are too faint to be detected in spectral images or do not cross the meridian, it is not possible to conclude whether the events are real continuum events. The events shown in Figure B.1 were indirectly recognized in the data as the script detected the neighbouring intense green auroral with emission from the first positive group of molecular nitrogen, which is highlighted. Figure B.2 shows events that are mostly embedded in a larger pink auroral structure. It is not possible to determine a spectrum for the green aurora in Figure B.2b due to dust on the CCD sensor.

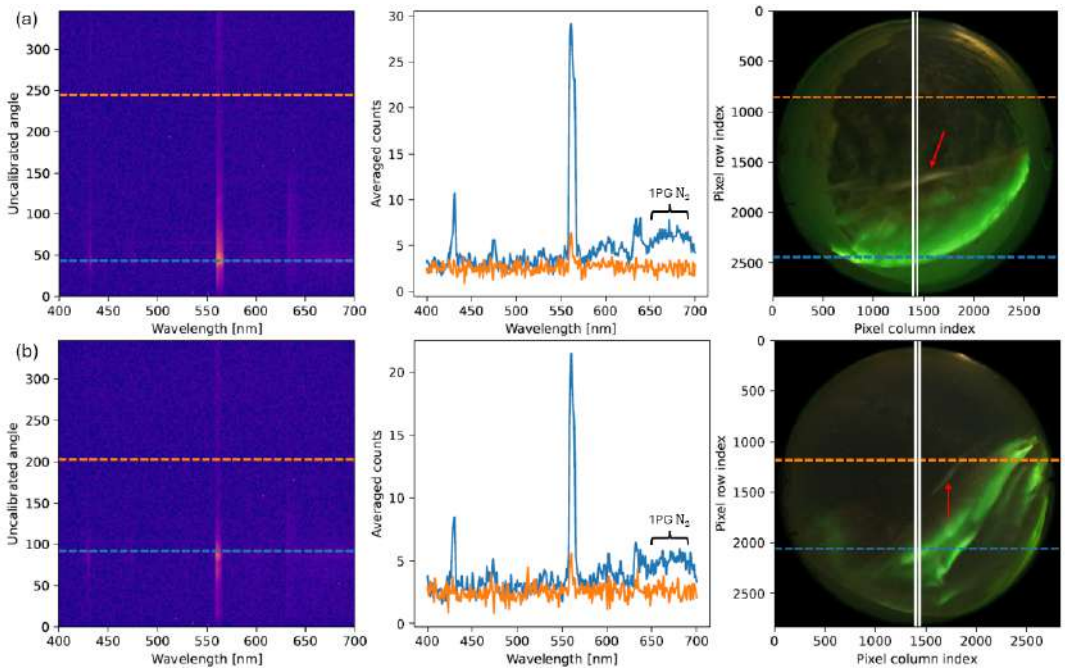

Figure B.1: MISS-1 spectral image, averaged detected and reference spectra and Sony A7s camera image for the possible thin continuum events, highlighted with red arrows, on (a) 01-01-2020 and (b) 22-02-2020. Spectral images are taken at (a) 22:16:00 UT and (b) 21:33:00 UT. Sony camera images are taken at (a) 22:16:03 UT and (b) 21:33:04 UT.

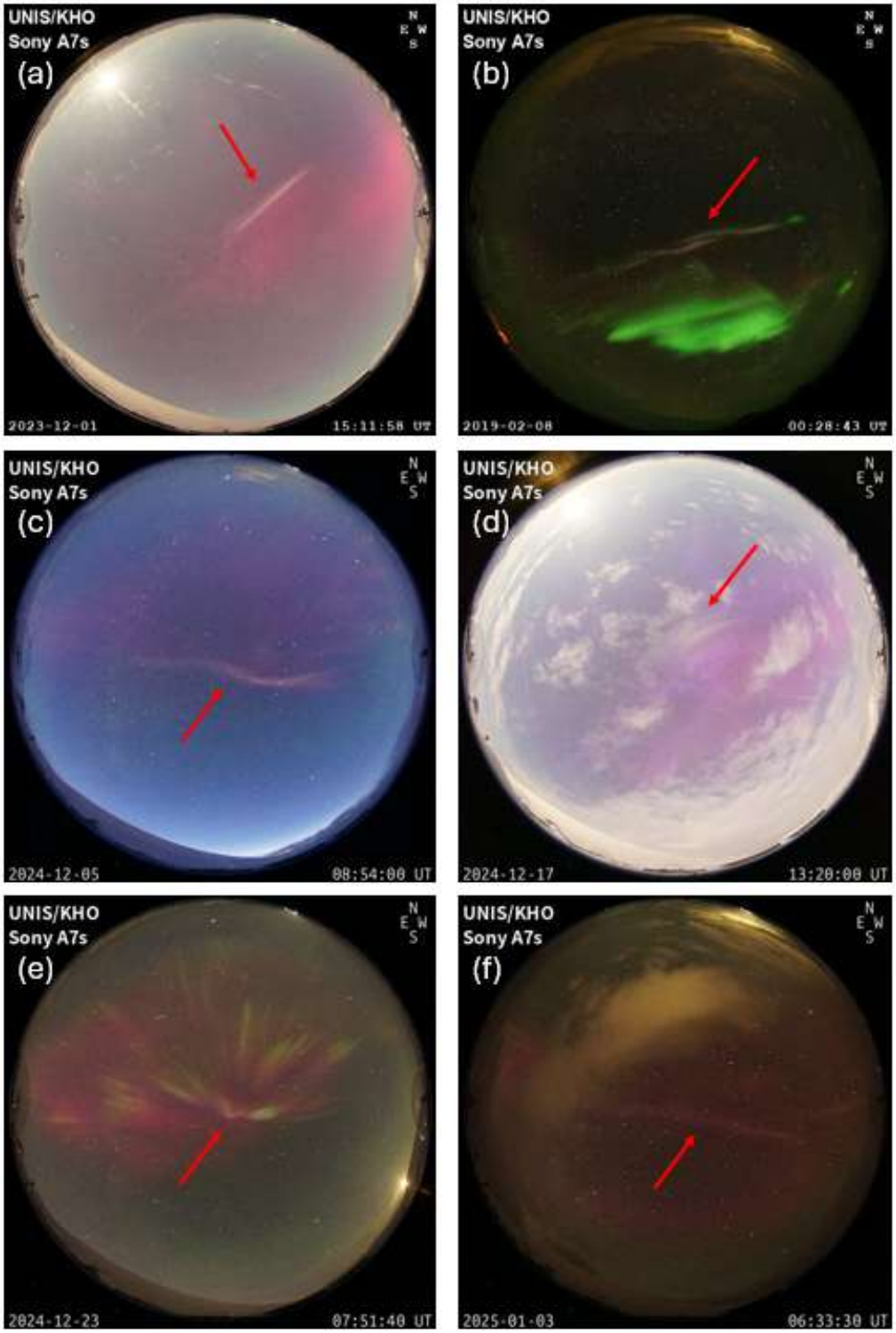

Figure B.2: Possible thin auroral continuum events, highlighted with red arrows, for which no spectral image is available. The continuum emission does not cross the meridian or is too faint to be detected. All events, except (b), are embedded in a larger pink auroral structure. The time and day of the Sony A7s camera image is shown in the bottom corners of each image. The events in (a) and (b) are mentioned by Partamies et al. [41].

B.2 Fake continuum events

This section contains a couple of examples of auroral events that the script identifies as possible continuum emission due to the apparent spectral enhancement with respect to the reference spectrum. In the case of the event in Figure B.3b it is expected that reflections from the moon cause this 'fake' enhancement in the spectrum. The event in Figure B.3a is more complicated as there is no direct light from the sun or moon visible, there is also little cloud cover. It could be that the spectrograph is saturated such that the spectral enhancement appears to be over the full wavelength range. However, continuum events observed on the nightside by Spanswick et al. have a similar spectrum without a clear white color in the image, hence it can not be ruled out that this is continuum emission [46].

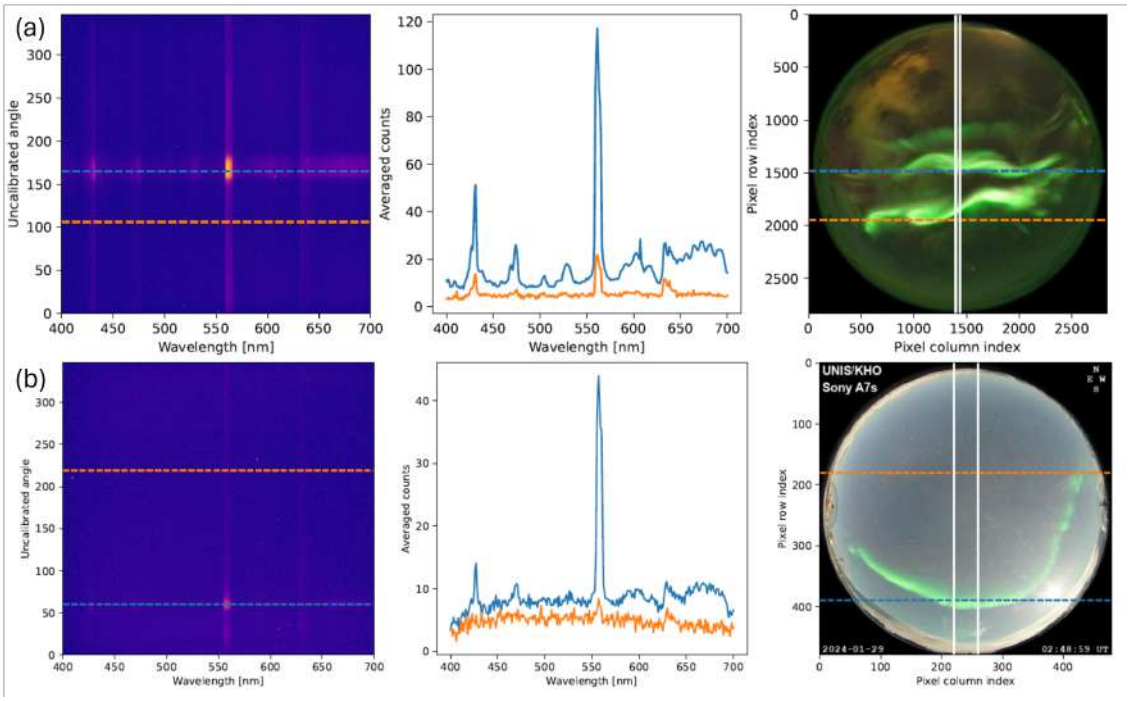

Figure B.3: MISS-1 spectral image, averaged detected and reference spectra and Sony A7s camera image for the possible fake continuum events on (a) 10-12-2018 and (b) 29-01-2024. Spectral images are taken at (a) 06:45:00 UT and (b) 02:49:00 UT. Sony camera images are taken at (a) 06:44:54 UT and (b) 02:48:59 UT.

Appendix C

Additional analysis ionospheric conditions

C.1 Keograms fat continuum events

Keograms of fat continuum events that were not specifically highlighted in the main text are shown here in Figure C.1. Periods where continuum emission is observed are highlighted with black lines, also indicating the shadow height during that interval. Following the main text, all events are observed between shadow heights of 120 - 200 km.

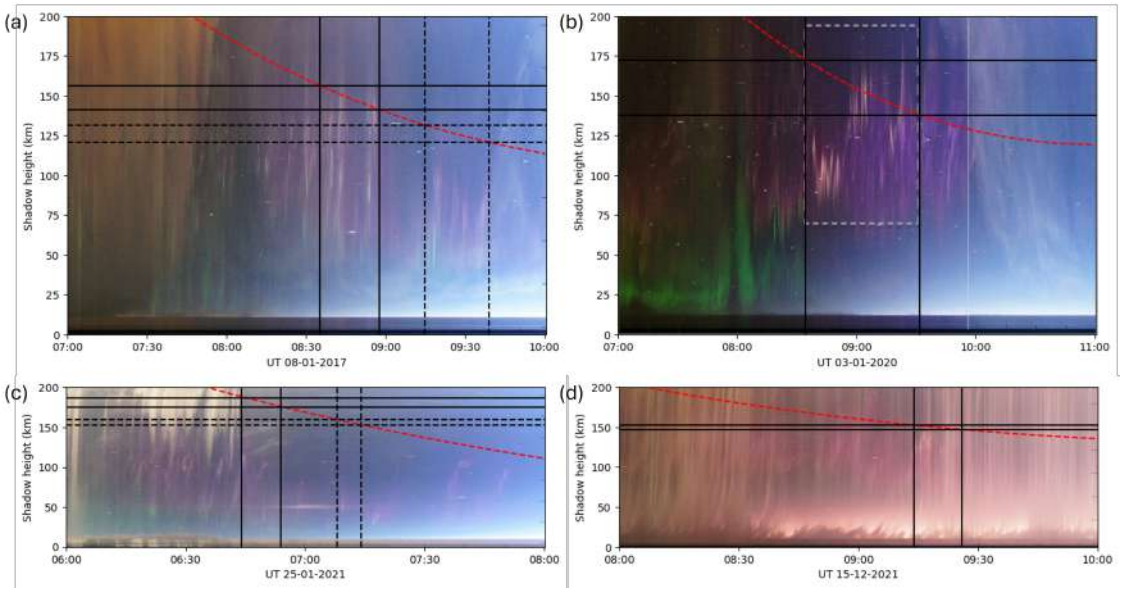

Figure C.1: Keograms from high resolution Sony A7s camera images for the fat continuum events on (a) 08-01-2017, (b) 03-01-2020, (c) 25-01-2020 and (d) 15-12-2021. The red dashed line shows the evolution of the shadow height in the ionosphere above KHO as a function of time. The black lines indicate the interval during which the fat continuum events are observed. The y-axis is not scaled to the keogram but to the red dashed line.

C.2 Temporal evolution ionospheric conditions

The evolution of ionospheric conditions for the fat continuum events shown in the previous section is shown in Figure C.2 and Figure C.3 during the same interval. Data on the AE, AL and AU indices is not available for the event on 03-01-2020. IMF data is not available for the event on 15-12-2021. Therefore, this is not shown in Figure C.2.

Overall, observations match with those described in the main text. All four fat continuum events occur as the SYM/H index declines and consequently the AL index declines, indicating enhanced ionospheric convection in the westward convection cell. The same treshold value of -100 nT for the AL index is identified. A high IMF magnitude is measured, making the onset of magnetic storms likely, especially in combination with previously identified strong particle precipitation. All four fat continuum events occur in the magnetic morning sector in the region of the westward convection cell, in agreement with the observed eastward flow. Furthermore, in all four events is the B_y component strongly negative, indicating a dawn-dusk asymmetry between the convection cells.

The black dashed line in Figure C.2 highlights the instance when the continuum emission observed on 03-01-2020 seems to abruptly diminish in intensity. This might be due to a sudden change in the B_y or B_z component or due to the magnetic storm entering the recovery phase. Fluctuations of several nanotesla are observed for the B_y and B_z component, which is possibly the origin of the 'bursty' nature of continuum emission due to aperiodic changes in magnetic reconnection, as explained in the main text.

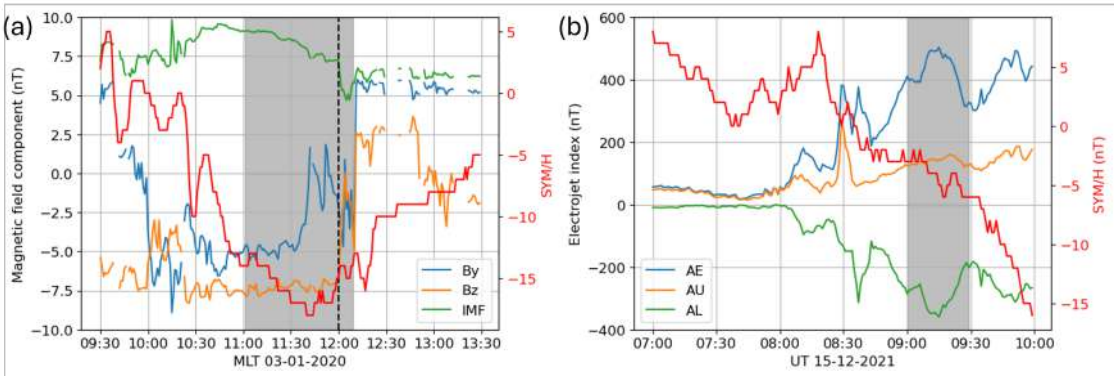

Figure C.2: (a) The By and Bz component of the IMF as well as the total IMF magnitude and SYM/H index as a function of magnetic local time (UT+2.5) on 03-01-2020. (b) The AE, AU, AL and SYM/H indeces as a function of time on 15-12-2021. Grey shaded areas highlight the observation of fat continuum emission. All data is 1 min averaged and magnetic field values are time-shifted to Earth's bow shock, from OMNIWeb [35].

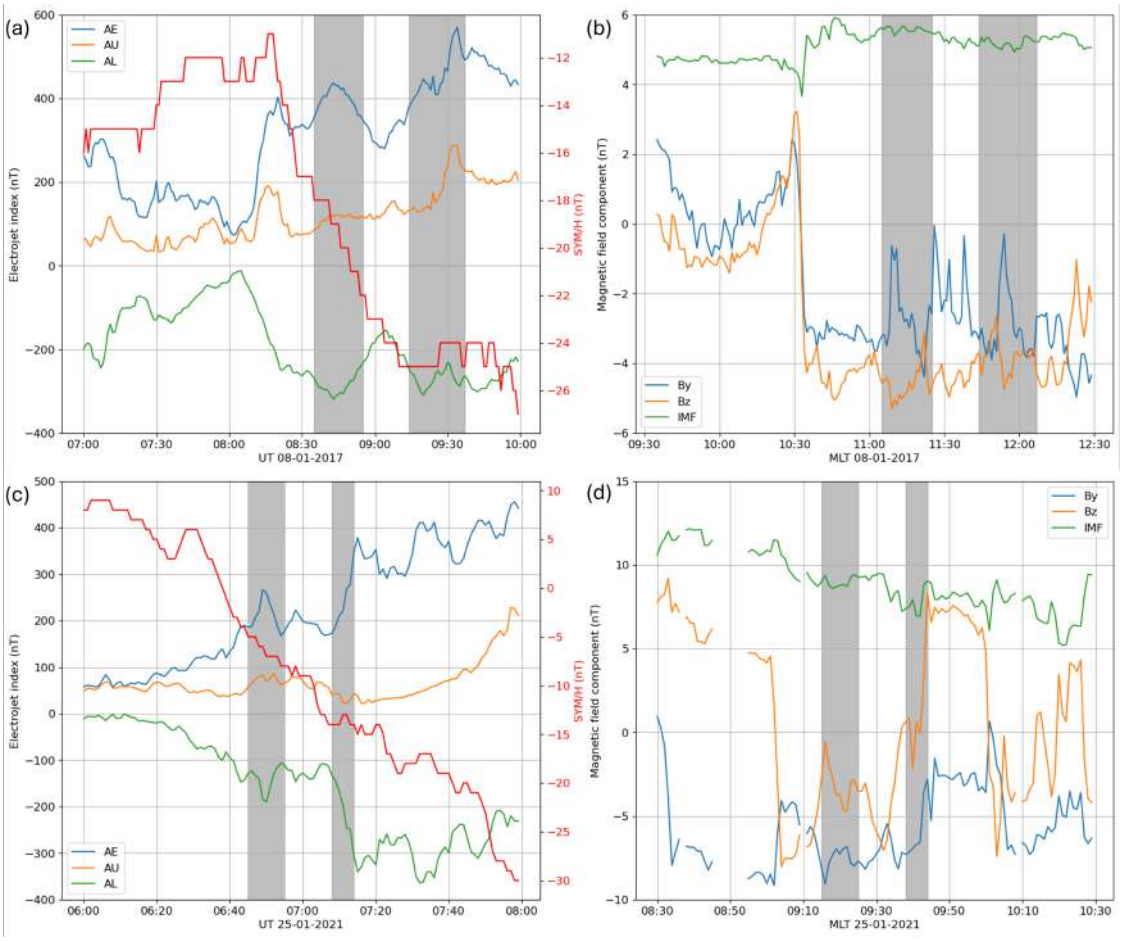

Figure C.3: (a) The AE, AU, AL and SYM/H indeces as a function of time on 08-01-2017. (b) The By and Bz component of the IMF as well as the total IMF magnitude as a function of magnetic local time (UT+2.5) on 08-01-2017, the same period as (a). (c) The same as (a) but on 25-01-2021. (d) Same as (c) but on 25-01-2021 with the same period as (c). Grey shaded areas highlight the observation of fat continuum emission. All data is 1 min averaged and magnetic field values are time-shifted to Earth's bow shock, from OMNIWeb [35].